






















Multi-wavelength Observations of AT2019wey: a New Candidate Black Hole Low-mass X-Ray Binary

Yuhan Yao ¹, S. R. Kulkarni ¹, Kevin B. Burdge ¹, Ilaria Caiazzo ¹, Kishalay De ¹, Dillon Dong ¹,
Mansi M. Kasliwal ¹, Thomas Kupfer ², Jan van Roestel ¹, Jesper Sollerman ³, Ashot Bagdasaryan,¹ Eric C. Bellm ⁴,
S. Bradley Cenko ⁵, Andrew J. Drake,¹ Dmitry A. Duev ¹, C. Fremling ¹, Matthew J. Graham ¹, Stephen Kaye,⁶
Frank J. Masci ⁷, Nicolas Miranda ⁸, Thomas A. Prince ¹, Reed Riddle ⁶, Ben Rusholme ⁷ and
Maayane T. Soumagnac ^{9,10}

¹Division of Physics, Mathematics and Astronomy, California Institute of Technology, Pasadena, CA 91125, USA

²Texas Tech University, Department of Physics & Astronomy, Box 41051, 79409, Lubbock, TX, USA

³The Oskar Klein Centre, Department of Astronomy, Stockholm University, AlbaNova, SE-10691 Stockholm, Sweden

⁴DIRAC Institute, Department of Astronomy, University of Washington, 3910 15th Avenue NE, Seattle, WA 98195, USA

⁵Astrophysics Science Division, NASA Goddard Space Flight Center, Greenbelt, MD 20771, USA

⁶Caltech Optical Observatories, California Institute of Technology, Pasadena, CA 91125, USA

⁷IPAC, California Institute of Technology, 1200 E. California Blvd, Pasadena, CA 91125, USA

⁸Institut für Informatik, Humboldt-Universität zu Berlin, Rudower Chaussee 25, 12489 Berlin, Germany

⁹Lawrence Berkeley National Laboratory, 1 Cyclotron Road, Berkeley, CA 94720, USA

¹⁰Department of Particle Physics and Astrophysics, Weizmann Institute of Science, Rehovot 76100, Israel

Abstract

AT2019wey (ATLAS19bcxp, SRGA J043520.9+552226, SRGE J043523.3+552234, ZTF19acwrvzk) is a transient reported by the ATLAS optical survey in December 2019, but shot to fame upon detection, three months later, by the *Spektrum-Roentgen-Gamma* (*SRG*) mission in its on-going sky survey. Here we present our ultraviolet, optical, near-infrared and radio observations of this object. Our X-ray observations are reported in a separate paper. We conclude that AT2019wey is a newly discovered Galactic low-mass X-ray binary (LMXB) and a candidate black hole (BH) system. Remarkably, we demonstrate that from ~ 58950 MJD to ~ 59100 MJD, despite the significant brightening in radio and X-ray (more than a factor of 10), the optical luminosity of AT2019wey only increased by 1.3–1.4. We interpret the bright UV/optical source in the dim low/hard state (~ 58950 MJD) as thermal emission from a truncated disk in a hot accretion flow, and the UV/optical emission in the hard-intermediate state (~ 59100 MJD) as reprocessing of X-ray flux in the outer accretion disk. We discuss the power of combining current wide-field optical surveys and *SRG* in the discovery of the emerging population of short-period BH LMXB systems with low accretion rates.

Keywords: X-rays: individual (AT2019wey) — accretion, accretion disks — stars: black holes

1. Introduction

Low-mass X-ray binaries (LMXBs) contain an accreting neutron star (NS) or black hole (BH) in orbit with a low mass ($\lesssim 1.4 M_{\odot}$) companion star. Most of the known black hole LMXBs are discovered by X-ray all-sky monitors (ASM) during their X-ray outbursts (also termed as the X-ray novae phenomena) induced by instabilities in the accretion processes. The most sensitive X-ray ASM to date, the Monitor of All-

sky X-ray Image (*MAXI*; Matsuoka et al. 2009), has a transient triggering threshold of 8 mCrab (1 mCrab = 2.4×10^{-11} erg s⁻¹ cm⁻² over 2–10 keV) for 4 d (Negoro et al. 2016). Due to the relatively shallow sensitivity of ASMs, the sample of LMXBs is biased to nearby sources with bright X-ray outbursts.

The first X-ray all sky survey was carried out in 1990/1991 by *ROSAT* (0.1–2.4 keV) (Truemper 1982; Voges et al. 1999). It cataloged X-ray sources brighter than $\sim 10 \mu\text{Crab}$, providing the deepest and cleanest X-ray all-sky reference prior to 2020 (Boller et al. 2016). Three decades after *ROSAT*, the dynamic X-ray sky is

being surveyed by the eROSITA (0.2–10 keV; [Merloni et al. 2012](#); [Predehl et al. 2020](#)) and the Mikhail Pavlinsky ART-XC (4–30 keV; [Pavlinksky et al. 2018](#)) telescopes on board the *Spektrum-Roentgen-Gamma* (*SRG*) mission. This planned four-year survey with full-sky images every six months also makes it a powerful time domain facility. The first eROSITA All-Sky Survey (eRASS1; December 2019 – June 2020) was sensitive to point sources down to $\sim 0.8 \mu\text{Crab}$ ([Predehl et al. 2020](#)). Therefore, eRASS1 is more than 10 times more sensitive than *ROSAT*.

During eRASS1, the discoveries of 15 X-ray transients were reported through the Astronomer’s Telegram (ATel) by *SRG*, with observed X-ray fluxes ranging from $6 \mu\text{Crab}$ to 12.5 mCrab . Among them, SRGA J043520.9+552226 (=SRGE J043523.3+552234) was discovered on 18 Mar 2020 ([Mereminskiy et al. 2020](#)). Its position is coincident with that of AT2019wey (ATLAS19bcxp), an optical transient reported to the Transient Name Server (TNS) in Dec 2019 ([Tonry et al. 2019](#)) by the ATLAS team ([Tonry et al. 2018](#)). This bright optical (17.5 mag) and X-ray (1 mCrab) source was not present in previous sky surveys such as the Palomar Observatory Sky Survey and the *ROSAT* sky survey. Motivated thus, we conducted an extensive follow-up campaign, revealing that AT2019wey is a Galactic LMXB with unique properties.

Yao et al. (in prep, hereafter Paper I) present a comprehensive X-ray report on AT2019wey from ~ 1 year prior to the optical discovery in Dec 2019 to 30 Sep 2020. AT2019wey appeared as a $\sim 1 \text{ mCrab}$ source in the low/hard-state (LHS) upon the optical discovery in Dec 2019, underwent a major X-ray brightening from $\sim 1 \text{ mCrab}$ to $\sim 25 \text{ mCrab}$ between June and August 2020, transitioned into the hard-intermediate state (HIMS) around $\sim 59082 \text{ MJD}$, and stayed in the HIMS until the end of September 2020.

In this work, we present multi-wavelength observations of AT2019wey, from which we conclude that the compact object is probably a black hole and the companion star must be of low mass ($< 0.8 M_{\odot}$). We therefore call AT2019wey a candidate BH LMXB. Review articles of this class of objects and the classification of their X-ray states can be found in literature ([McClintock & Remillard 2006](#); [Remillard & McClintock 2006](#); [Belloni et al. 2011](#); [Zhang 2013](#)).

The paper is organized as follows. Section 2 outlines the association between the optical and X-ray transients. We present historical and new photometry in optical and ultraviolet (UV) bands in Section 3. We describe optical and near-infrared (NIR) spectroscopy in Section 4. Section 5 shows radio follow-up observations. Section 6

provides a panchromatic analysis, from which we infer the origin of the optical/UV radiation. We discuss constraints on the companion mass and orbital period of AT2019wey in Section 7. We conclude in Section 8. UT time is used throughout the paper.

2. Association between the Optical and X-ray Transients

The *SRG* detection of SRGE J043523.3+552234 provided a localization shown by the white plus sign in Figure 1, where the circle marks eROSITA’s 68% error circle radius of $\sim 5''$ ([Mereminskiy et al. 2020](#)). The optical transient ATLAS19bcxp (AT2019wey) was discovered by the ATLAS ([Tonry et al. 2018](#)) optical survey and reported to TNS on 7 Dec 2019 ([Tonry et al. 2019](#)), and the optical source was also detected by the Zwicky Transient Facility (ZTF; [Bellm et al. 2019b](#); [Graham et al. 2019](#)). The median of all ZTF detection positions of AT2019wey is shown as the cross sign in Figure 1.

Table 1. Position of AT2019wey.

eROSITA coordinate	ra = $68.8472 \pm 0.0024^{\circ}$ dec = $55.3760 \pm 0.0014^{\circ}$
ZTF coordinate	ra = $68.846966 \pm 0.000014^{\circ}$ dec = $55.376193 \pm 0.000008^{\circ}$
Galactic coordinate	$l = 151.16113^{\circ}$, $b = 5.29973^{\circ}$

In the Sloan Digital Sky Survey (SDSS, [Alam et al. 2015](#)) database, the nearest point source to SRGE J043523.3+552234 is to the northeast outside of the eROSITA error circle (Figure 1), and we therefore exclude an association. The optical transient AT2019wey and the X-ray transient SRGE J043523.3+552234 are just $0.8''$ off each other, confirming the association suggested by [Mereminskiy et al. \(2020\)](#). We give the J2000 position of AT2019wey in Table 1.

3. Photometry

3.1. Historical Photometry

We conducted an archival search of optical photometry at the position of AT2019wey. The source was not detected by historical optical surveys, including the Palomar Observatory Sky Survey I (POSS-I, [Minkowski & Abell 1963](#)), the Second Palomar Observatory Sky Survey (POSS-II, [Reid et al. 1991](#)), SDSS, and the Panoramic Survey Telescope and Rapid Response System (Pan-STARRS, PS1) DR1 ([Flewelling et al. 2016](#); [Waters et al. 2016](#)), the intermediate Palomar Transient Factory (iPTF; [Rau et al. 2009](#); [Law et al. 2009](#)), and the ZTF. We list $5\text{-}\sigma$ upper limits in Table 2.

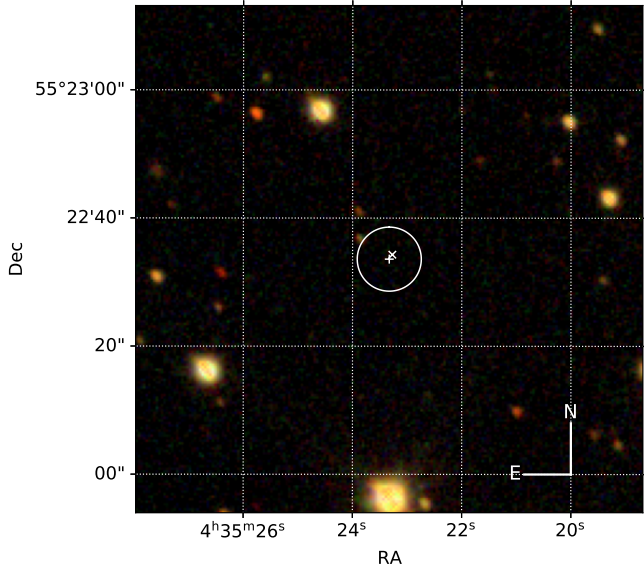


Figure 1. Localization of AT2019wey plotted on top of a color image constructed with SDSS *gri* images using the prescription in Lupton et al. (2004). The eROSITA position is shown by the white plus (“+”) sign, and the ZTF position is shown by the white cross sign (“×”). The white circle indicates eROSITA’s 68% error circle radius of 5″.

Table 2. Historical upper limits at the position of AT2019wey.

Survey	Time	Filter	λ_{eff} (Å)	Limit (mag)
POSS-I	1953-10-08	<i>r</i>	6500 Å	19.5
POSS-II	1990-10-26	<i>r</i>	6500	20.8
SDSS	2004-10-15	<i>u</i>	4720	24.6
SDSS	2004-10-15	<i>g</i>	6200	25.7
SDSS	2004-10-15	<i>r</i>	6190	24.8
SDSS	2004-10-15	<i>i</i>	7500	24.1
SDSS	2004-10-15	<i>z</i>	8960	23.5
PS1	2013-01-27	<i>r</i>	6800	23.3
iPTF	2014-01-24	<i>R</i>	6420	21.0
ZTF	2017-12–2019-11	<i>g</i>	4810	21.3
ZTF	2017-12–2019-11	<i>r</i>	6420	21.5

NOTE—Limit magnitude is given in the AB system.

3.2. New Optical Photometry

3.2.1. ZTF Photometry

ZTF conducts multiple time-domain surveys (Bellm et al. 2019a) using the ZTF mosaic camera (Dekany et al. 2020) on the the Palomar Oschin Schmidt 48-inch (P48) telescope. Following Yao et al. (2019), we performed forced point-spread-function (PSF) photometry on ZTF difference images generated with the ZTF real-

time reduction and image subtraction pipeline (Masci et al. 2019). Images obtained after December 2019 as part of the ZTF public survey have not been released, preventing us from applying our forced-PSF measurements. We therefore use photometry reported in real-time alert packets (Patterson et al. 2019) for ZTF observations obtained under the public survey (Table 3).

Figure 2 shows the ZTF light curve of AT2019wey, as well as the ATLAS detection. The first ZTF forced photometry detection was on 2019 Dec 2 05:19:40.8 (JD = 2458819.722) for a *g*-band detection at 19.15 ± 0.05 mag. The last non-detection was on 2019 Nov 25 07:14:52.8 (JD = 2458812.802) for a *r*-band limit at 21.21 mag. It is shown (see the inset of Figure 2) that the *r*-band light curve rose from > 21.2 mag to 17.4 mag in ~ 15 days. After that, the light curve displays small amplitude ($\lesssim 0.3$ mag) variability for more than 300 days. The lack of photometry between ~ 58580 MJD to ~ 59030 MJD is due to the source being in the day sky.

Table 3. ZTF P48 Photometry of A2019wey.

MJD	<i>m</i>	σ_m	Filter	Photometry
58819.2213	19.308	0.116	<i>g</i>	alert
58819.2220	19.154	0.052	<i>g</i>	forced
58819.2827	18.555	0.096	<i>r</i>	alert
58819.2860	18.548	0.028	<i>r</i>	forced
58820.2180	18.724	0.122	<i>g</i>	forced
58827.2550	17.447	0.019	<i>r</i>	forced
58827.2576	17.415	0.047	<i>r</i>	alert
58827.2651	17.396	0.048	<i>r</i>	alert
58828.2550	17.635	0.116	<i>r</i>	forced
58828.4580	18.112	0.080	<i>g</i>	forced

NOTE—*m* and σ_m are observed magnitude (without extinction correction) in the AB system. The last column indicates method of the magnitude measurement (alert packets or forced photometry). Data up to 1 Nov 2020 is included. (This table is available in its entirety in machine-readable form.)

3.2.2. CHIMERA Photometry

On 23 July 2020 we obtained high speed photometry in the SDSS *g*- and *i*-band using the Caltech High-speed Multi-color camera (CHIMERA; Harding et al. 2016) on the 200-inch Hale telescope of the Palomar observatory. We operated the detectors using the 1 MHz conventional amplifier in frame transfer mode with a frame exposure time of 1 s, and obtained 3300 frames in each filter. We reduced the data with a custom in

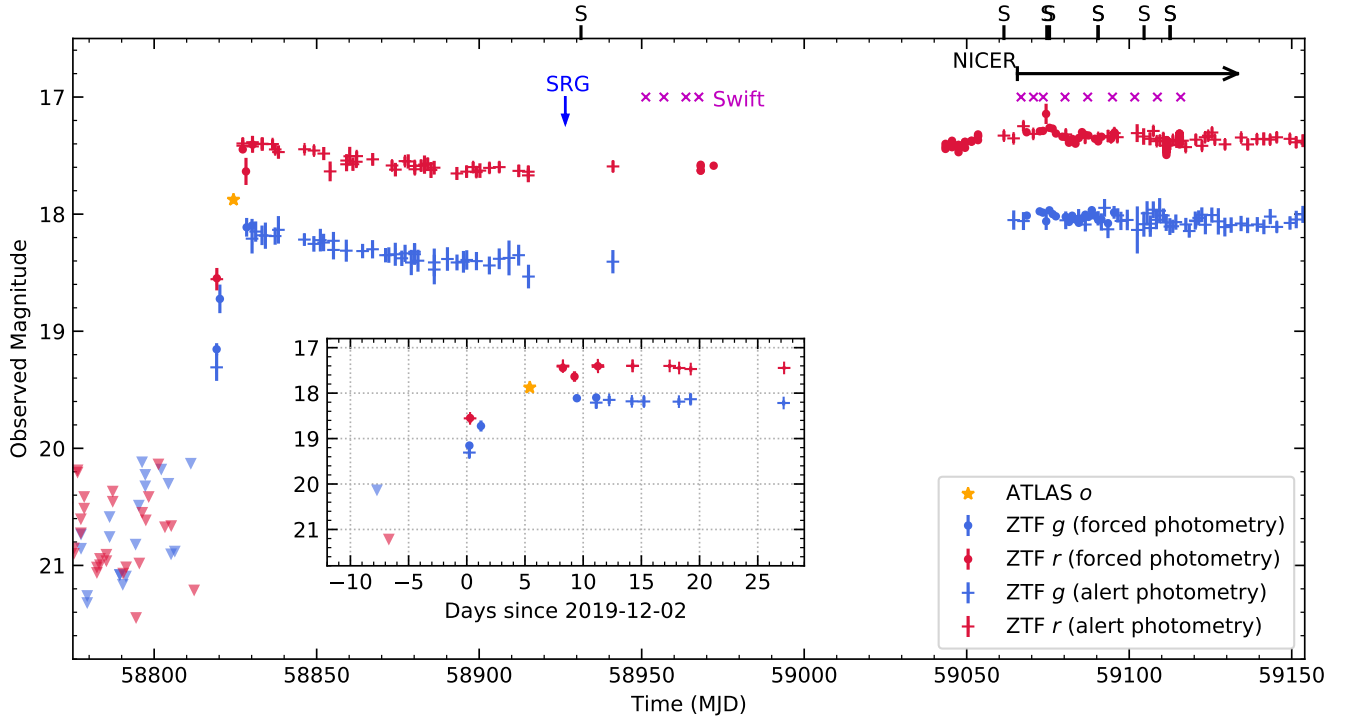


Figure 2. Optical light curve of AT2019wey. The inset shows the light curve zoomed around the first ZTF detection epoch. Upper limits are shown as downward triangles. Epochs of *SRG* discovery and *Swift* observations are marked by the blue arrow and magenta crosses, respectively. Along the upper axis, epochs of spectroscopy (Table 6) are marked with the letter S above the axis. AT2019wey has been monitored by the *Neutron Star Interior Composition Explorer* (*NICER*; Gendreau et al. 2016) starting from 04 Aug 2020.

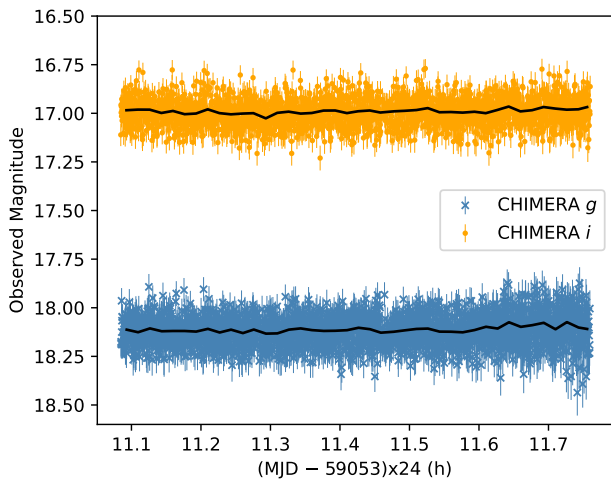


Figure 3. CHIMERA data of AT2019wey. The black lines show light curves averaged to 1 min.

house pipeline¹. AT2019wey was detected at a median of 16.99 mag (rms = 0.07 mag) in *i*-band, and at a me-

dian of 18.12 mag (rms = 0.08 mag) in *g*-band. The *g*-band rms increased towards the end of the observation due to the onset of twilight. Figure 3 shows the CHIMERA light curve.

3.3. UV Photometry

We obtained ultraviolet (UV) observations of AT2019wey with the Ultra-Violet/Optical Telescope (UVOT; Roming et al. 2005) onboard the *Neil Gehrels Swift Observatory* (Gehrels et al. 2004). A summary of *Swift* observations is given in Table 4. The UVOT data was processed using HEASOFT version 6.27. For the three epochs of observations obtained in Apr 2020, AT2019wey was not detected above $3\text{-}\sigma$ in individual exposures of the UV filters (including *U*, *uvm2*, *uvw1*, and *uvw2*). Therefore, for each filter, we coadded the three exposures using *uvotsum* and extracted the photometry with *uvotsource* using a $3''$ circular aperture. Background counts were estimated in a $10''$ source-free circular aperture. After that, the source was detected with $\sim 7\text{-}\sigma$ in the *V* and *B* filters, $\sim 4\text{-}\sigma$ in the *U* and *uvw1* filters, and $\sim 2.5\text{-}\sigma$ in the *uvm2* and *uvw2* filters. For UV data taken in Aug–Sep 2020, we did not coadd and present $> 3\text{-}\sigma$ detections in Table 5.

¹ <https://github.com/mcoughlin/kp84>

Table 4. Log of *Swift* Observations.

Observation Time (UTC)	Exp. (s)	UVOT filters
2020-04-12T06:07:20	1523	—
2020-04-17T19:55:12	874	<i>uvw2 uvm2 uvw1 U B V</i>
2020-04-24T14:28:39	1026	<i>uvw2 uvm2 uvw1 U B V</i>
2020-04-28T13:56:23	1043	<i>uvw2 uvm2 uvw1 U B V</i>
2020-08-05T17:16:06	222	—
2020-08-09T13:17:40	846	<i>uvm2</i>
2020-08-12T13:10:03	1181	<i>uvw2</i>
2020-08-19T05:53:06	998	<i>U</i>
2020-08-26T05:17:00	1006	<i>uvw1</i>
2020-09-02T20:36:23	434	<i>uvm2</i>
2020-09-09T16:40:49	1023	<i>uvw2</i>
2020-09-16T16:01:34	858	<i>U</i>
2020-09-23T20:03:15	794	<i>uvw1</i>

Table 5. UV photometry for AT2019wey.

Date	Instrument	Filter	m
2020-04 Coadd	<i>Swift</i> /UVOT	<i>B</i>	18.92 ± 0.16
2020-04 Coadd	<i>Swift</i> /UVOT	<i>U</i>	20.17 ± 0.24
2020-04 Coadd	<i>Swift</i> /UVOT	<i>uvm2</i>	22.63 ± 0.42
2020-04 Coadd	<i>Swift</i> /UVOT	<i>uvw1</i>	21.28 ± 0.27
2020-04 Coadd	<i>Swift</i> /UVOT	<i>uvw2</i>	22.99 ± 0.49
2020-04 Coadd	<i>Swift</i> /UVOT	<i>V</i>	17.95 ± 0.15
2020-08-09	<i>Swift</i> /UVOT	<i>uvm2</i>	21.86 ± 0.31
2020-08-12	<i>Swift</i> /UVOT	<i>uvw2</i>	21.50 ± 0.21
2020-08-19	<i>Swift</i> /UVOT	<i>U</i>	19.32 ± 0.06
2020-08-26	<i>Swift</i> /UVOT	<i>uvw1</i>	20.49 ± 0.13
2020-09-02	<i>Swift</i> /UVOT	<i>uvm2</i>	> 21.62
2020-09-09	<i>Swift</i> /UVOT	<i>uvw2</i>	21.68 ± 0.24
2020-09-16	<i>Swift</i> /UVOT	<i>U</i>	19.26 ± 0.07
2020-09-23	<i>Swift</i> /UVOT	<i>uvw1</i>	20.40 ± 0.13
2020-10-21	P60/SEDM	<i>U</i>	19.11 ± 0.09
2020-10-25	P60/SEDM	<i>U</i>	19.21 ± 0.31

NOTE— m and σ_m are observed magnitude (without extinction correction) in the AB system. The UV light curve is presented in Figure 11.

In Oct 2020, we also obtained *U*-band photometry using the Spectral Energy Distribution Machine (SEDM, Blagorodnova et al. 2018, Rigault et al. 2019) on the robotic Palomar 60-inch telescope (P60, Cenko et al.

2006). Data reduction was performed using the Fremling Automatic Pipeline (Fremling et al. 2016). The reduced photometry is also presented in Table 5.

4. Optical and NIR Spectroscopy

We obtained optical spectroscopic follow-up observations of AT2019wey using the Double Spectrograph (DBSP; Oke & Gunn 1982) on the 200-inch Hale telescope, the Low Resolution Imaging Spectrograph (LRIS; Oke et al. 1995) on the Keck-I telescope, and the Echelle Spectrograph and Imager (ESI) on the Keck-II telescope. We obtained NIR spectroscopy using the Near infrared emission spectroscopy (NIREs) on the Keck-II telescope. Spectroscopic observations were coordinated with the GROWTH Marshal (Kasliwal et al. 2019).

A log of our spectroscopic observations is given in Table 6. The DBSP spectra were reduced using the `pyraf-dbsp` pipeline (Bellm & Sesar 2016). The LRIS spectrum was reduced and extracted using `Lpipe` (Perley 2019). The flat-fielding, wavelength solution (using sky lines) and extraction for the NIREs spectra were carried out using the `spextool` code (Cushing et al. 2004). The extracted spectra were flux calibrated using the telluric A0V standard star HIP 16652 with the `xtellcor` code (Vacca et al. 2003). The ESI spectrum was reduced using the `MAKEE`² pipeline following the standard procedure. Flux calibration was not performed on the ESI spectrum.

4.1. Optical Spectroscopy

4.1.1. Overview

The LRIS spectrum obtained on 2020-03-23 is shown in the top panel of Figure 4. We identified prominent H I Balmer absorption lines, Ca II H and K lines, Na I D doublets, DIB $\lambda 5780$, $\lambda 6283$ absorption features, and Balmer jump at redshift $z = 0$. These features are present in all optical spectra (Figure 5). We tentatively detected He II $\lambda 4686$ emission in the spectra obtained on July 31, Aug 14, and Sep 20. We therefore conclude that AT2019wey is a transient of Galactic stellar origin. This is not surprising given the low Galactic latitude of this source (Table 1).

We note that during our observations, the blue end of DBSP’s red side CCD had a malfunction, such that flux in the ~ 5650 – 5750 Å wavelength range was lost. This problem also affects flux calibration of DBSP spectra from ~ 5750 Å to ~ 6200 Å. From the bottom panel of Figure 5, one can see that the DBSP spectra contain non-astrophysical structures between ~ 5700 Å to

² http://www.astro.caltech.edu/~tb/ipac_staff/tab/makee/

Table 6. Log of AT2019wey spectroscopy.

Start Time (UTC)	Instrument	Exp. (s)	Airmass	Resolution (FWHM) (\AA)
2020-03-23 07:44:47	Keck-I+LRIS	300	2.22	6
2020-07-31 10:52:40	P200+DBSP	600	1.38	5
2020-08-13 15:19:31	Keck-II+NIRES	360	1.38	6
2020-08-14 11:24:16	P200+DBSP	600	1.34	5
2020-08-29 09:59:22	P200+DBSP	600	1.42	5
2020-08-29 10:09:43	P200+DBSP	600	1.39	5
2020-09-12 13:41:51	Keck-II+ESI	1800	1.32	2
2020-09-20 13:07:31	Keck-I+LRIS	300	1.33	6
2020-09-20 14:40:27	Keck-I+LRIS	300	1.23	6

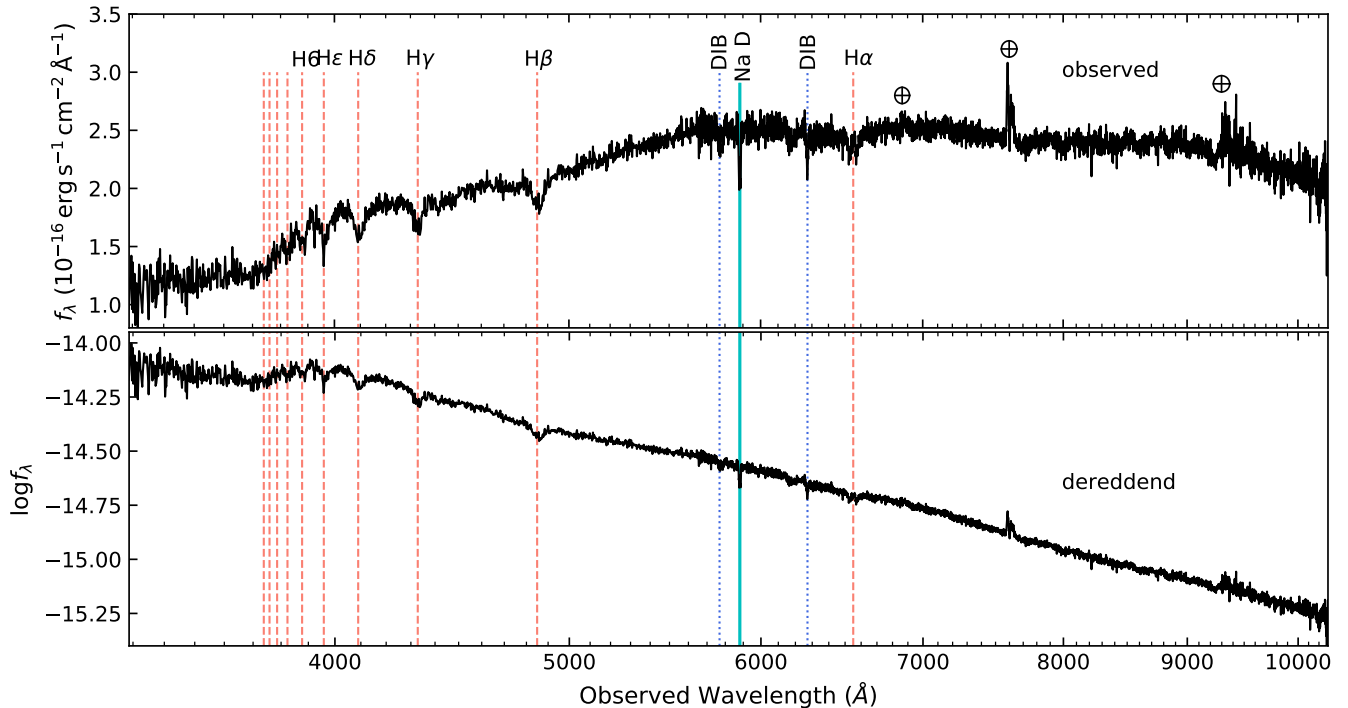


Figure 4. LRIS spectrum of AT2019wey obtained on 23 Mar 2020. *Upper:* observed spectrum. *Bottom:* extinction-corrected spectrum using $E(B - V) = 0.9$ mag. We mark rest (air) wavelength of atomic transitions in vertical lines. Dashed salmon: Balmer series. Solid cyan: Na I D doublet. Dotted blue: DIB absorptions.

$\sim 6200 \text{ \AA}$ in the continuum caused by the malfunction mentioned above, preventing equivalent width (EW) of spectral lines from being accurately determined. Furthermore, the quality of DBSP spectra is generally lower than that from the Keck telescopes. Therefore, in the analysis below, we only measure the EW from the LRIS and ESI spectra.

4.1.2. Extinction Estimation

Jenniskens & Desert (1994) shows that the diffuse interstellar band (DIB) $\lambda 5780$ and $\lambda 6283$ contain two blended components, a deep narrow absorption core superimposed on a shallow broad absorption feature. The two components are not resolved in our spectra. As of central wavelength of the DIB features, we adopt the values estimated by Hobbs et al. (2008): 5780.48 \AA for the narrow component of the DIB $\lambda 5780$, and 6283.83 \AA for

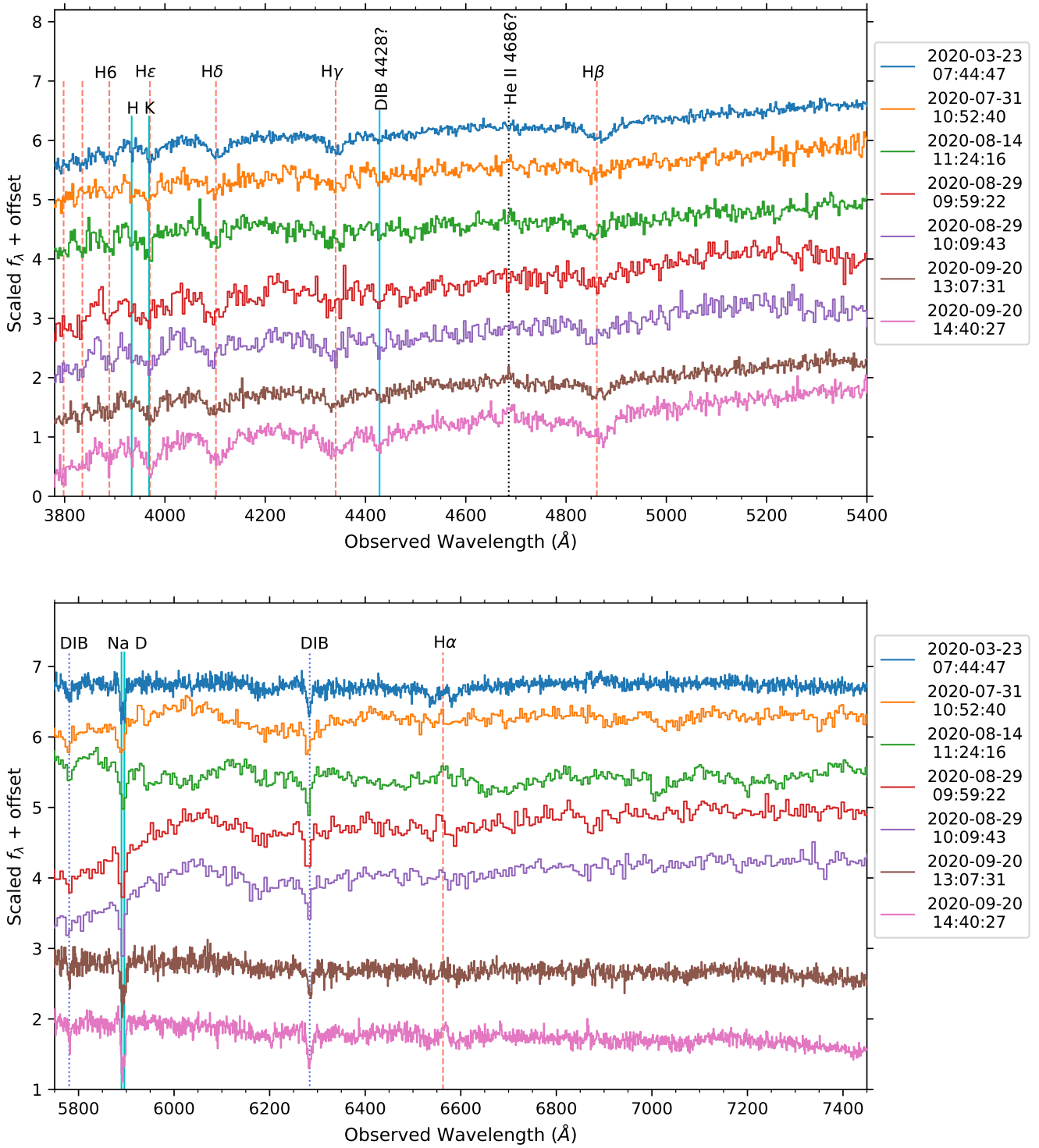


Figure 5. Zoom in on the blue and red portion of the seven low-resolution optical spectra (Table 6).

Table 7. Line Index Definition.

Name	Index Bandpass (Å)	Shoulder Bandpasses (Å)
DIB λ 5780	5774–5786	5755–5770, 5790–5805
Na I D	5879–5905	5856–5872, 5911–5925
Na I D1	5894.0–5897.5	5891.7–5893.9, 5897.6–5900.6
Na I D2	5887.9–5891.4	5884.7–5887.7, 5891.7–5893.9
DIB λ 6283	6267–6295	6247–6263, 6299–6313

NOTE—Wavelength is given in air.

Table 8. Line Index Measurements.

Name	Start Time (UTC)	EW (Å)	$E(B - V)$ (mag)
DIB λ 6283	2020-03-23 07:44:47	1.41 ± 0.13	1.12 ± 0.10
	2020-09-12 13:41:51	1.53 ± 0.06	1.21 ± 0.05
	2020-09-20 13:07:31	1.60 ± 0.16	1.27 ± 0.12
	2020-09-20 14:40:27	1.43 ± 0.05	1.14 ± 0.09
Na I D	2020-03-23 07:44:47	1.86 ± 0.11	2.12 ± 0.72
	2020-09-12 13:41:51	1.84 ± 0.08	2.00 ± 0.55
	2020-09-20 13:07:31	2.30 ± 0.16	6.96 ± 3.34
	2020-09-20 14:40:27	1.50 ± 0.09	0.81 ± 0.25
Na I D1	2020-09-12 13:41:51	0.85 ± 0.03	2.17 ± 0.90
Na I D2	2020-09-12 13:41:51	1.07 ± 0.03	2.48 ± 0.92
DIB λ 5780	2020-03-23 07:44:47	0.49 ± 0.10	0.80 ± 0.16
	2020-09-12 13:41:51	0.76 ± 0.09	1.25 ± 0.15
	2020-09-20 13:07:31	0.36 ± 0.18	0.60 ± 0.30
	2020-09-20 14:40:27	0.42 ± 0.06	0.69 ± 0.10

the narrow component of the DIB λ 6283 line. Relations between EW of the DIB lines and magnitudes of line-of-sight extinction are investigated by Yuan & Liu (2012):

$$EW(5780) = 0.61 \times E(B - V) \quad (1a)$$

$$EW(6283) = 1.26 \times E(B - V) \quad (1b)$$

The doublet absorption strength of Na I D $\lambda\lambda$ 5890, 5896 is also generally expected to correlate with the amount of dust along the line of sight. Poznanski et al. (2012) show that:

$$\log(E(B - V)) = 2.16 \times EW(D_2) - 1.91 \pm 0.15 \quad (2a)$$

$$\log(E(B - V)) = 2.47 \times EW(D_1) - 1.76 \pm 0.17 \quad (2b)$$

$$\log(E(B - V)) = 1.17 \times EW(D) - 1.85 \pm 0.08 \quad (2c)$$

where $EW(D) = EW(D_1) + EW(D_2)$. We measure the EW of DIB and Na I D lines in our LRIS and ESI spectra. The definition of line indices is given in Table 7. Table 8 presents the result. $EW(\text{DIB } \lambda 6283)$

and $EW(\text{DIB } \lambda 5780)$ are consistent with being constant across the four observing epochs. $EW(\text{Na I D})$ might exhibit variable line strength.

Using Eq. (1) and Eq. (2), we convert the measurements of EW into $E(B - V)$, which are shown in Table 8. The inverse variance weighted average is $E(B - V) = 1.19 \pm 0.04$ mag using $EW(\text{DIB } \lambda 6283)$, $E(B - V) = 1.14 \pm 0.22$ mag using $EW(\text{Na I D})$, and $E(B - V) = 0.83 \pm 0.07$ mag using $EW(\text{DIB } \lambda 5780)$. These estimations are close to each other, and are slightly greater than the total Galactic extinction of $E(B - V) = 0.88$ mag along the line-of-sight to AT2019wey estimated from Schlafly & Finkbeiner (2011). However, we note that at the measured EW , the number of stars in the sample used to yield Eq. (1) and Eq. (2) is very small, such that the calibration uncertainty is large. From the top panels of Figure 4 in Yuan & Liu (2012), we infer that $E(B - V)$ towards AT2019wey should be $\gtrsim 0.8$ mag. From the bottom panel of Figure 9 in Poznanski et al. (2012), we infer that $E(B - V)$ towards AT2019wey should be $\gtrsim 0.7$ mag.

We also attempt to infer the extinction by assuming that the 6000–10000 Å LRIS spectrum is in the Rayleigh-Jeans (RJ) tail of a blackbody spectrum ($f_\lambda \propto \lambda^{-4}$ when $h\nu \ll kT$), which yields $E(B - V) = 1.29$ mag. and a blackbody radius (R_{bb}) of

$$R_{\text{bb}} = (4.5 \times 10^{10} \text{ cm}) \left(\frac{D}{5 \text{ kpc}} \right) \left(\frac{T_{\text{bb}}}{5.0 \times 10^4 \text{ K}} \right)^{-1/2} \quad (3)$$

Note that this is likely an overestimate of the true extinction (and a lower limit of the outer disk radius), since the optical is only in the RJ limit when $kT \gg 2 \text{ eV}$ ($T \gg 2 \times 10^4 \text{ K}$). For instance, for an extinction of $E(B - V) \sim 0.9$ mag, we have

$$R_{\text{bb}} = (1.0 \times 10^{11} \text{ cm}) \left(\frac{D}{5 \text{ kpc}} \right) \left(\frac{T_{\text{bb}}}{1.1 \times 10^4 \text{ K}} \right)^{-1/2} \quad (4)$$

In summary, the extinction is inferred to be $0.8 \lesssim E(B - V) \lesssim 1.2$ mag. In the bottom panel of Figure 4, we dereddened the observed spectrum assuming $E(B - V) = 0.9$ mag, $R_V = 3.1$, and adopting the reddening law from Cardelli et al. (1989). The dereddened spectrum shows a blue continuum, with broad Balmer absorptions being the most prominent spectral lines.

4.1.3. Hydrogen Lines

From 23 Mar 2020 to 29 Aug 2020, the hydrogen profile clearly changes. As can be seen in the bottom panel of Figure 5, there is very strong H α absorption on 23

March 2020. In comparison, in the two LRIS spectra obtained on 20 Sep 2020, the absorption component is much weaker.

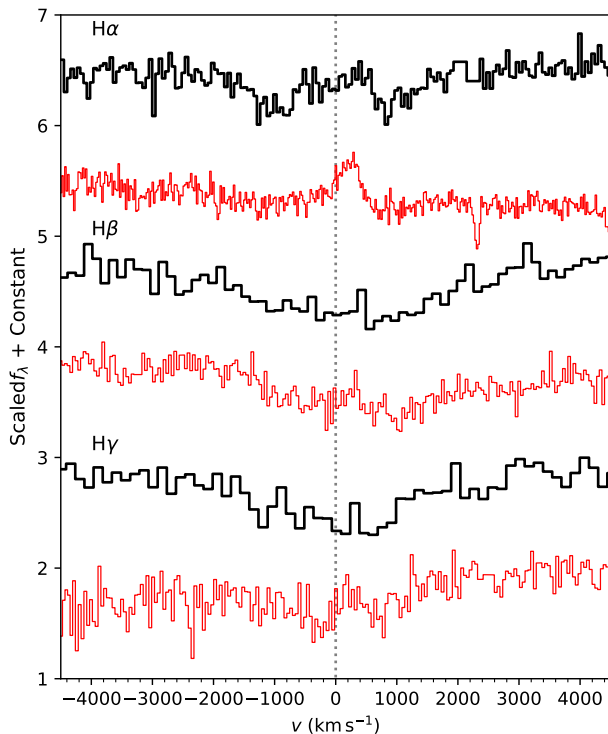


Figure 6. Velocity of the Balmer lines $H\alpha$, $H\beta$, and $H\gamma$ (from top to bottom). The thick black and thin red lines are from the 2020-03-23 LRIS spectrum and the 2020-09-12 ESI spectrum, respectively.

Figure 6 presents the velocity of lower series Balmer lines in the 23 March 2020 low resolution LRIS and the 12 Sep 2020 medium resolution ESI spectra. In the LRIS spectrum, we observe two absorption components around $H\alpha$. Such a profile may result from a relatively narrower ($\text{FWHM} \sim 1200 \text{ km s}^{-1}$) emission component in the middle of a rotationally broadened ($\text{FWHM} \sim 2700 \text{ km s}^{-1}$) shallow absorption trough. At the same epoch, we also observe broad $H\beta$ and $H\gamma$ lines with $\text{FWHM} \sim 2000\text{--}3000 \text{ km s}^{-1}$. There is a marginal detection of narrow emission cores redshifted by $\sim 300\text{--}400 \text{ km s}^{-1}$ from the line center of the absorption troughs. In the ESI spectrum, we observe flat-topped $H\alpha$ in emission ($\sim 400 \text{ km s}^{-1}$), while the $H\beta$ and $H\gamma$ profiles are similar to the $H\alpha$ profile in the LRIS spectrum.

The hydrogen lines in AT2019wey display both broad absorption and emission components. This behavior is reminiscent of some LMXBs and cataclysmic variables (CVs), where the hydrogen absorption and emis-

sion lines are thought to arise from different layers of the viscous accretion disk (Horne & Marsh 1986; La Dous 1989; Warner 1995). In a few BH LMXBs, double-peaked $H\alpha$ is observed, such as GRO J1655–40 (Soria et al. 2000), GRO J0422+32 (Callanan et al. 1995) XTE J1118+480 (Dubus et al. 2001; Torres et al. 2002) and Swift J1753.5–0127 (Rahoui et al. 2015). The single-peaked hydrogen line profile of AT2019wey is similar to that observed in MAXI J1836–194 (Russell et al. 2014), suggesting a binary system with relatively low inclination (i.e., close to face-on), which is in agreement with modeling of the X-ray reflection spectrum (Paper I). We further discuss reasons for the variable Balmer lines in Section 6.3.4.

4.1.4. Distance Estimation

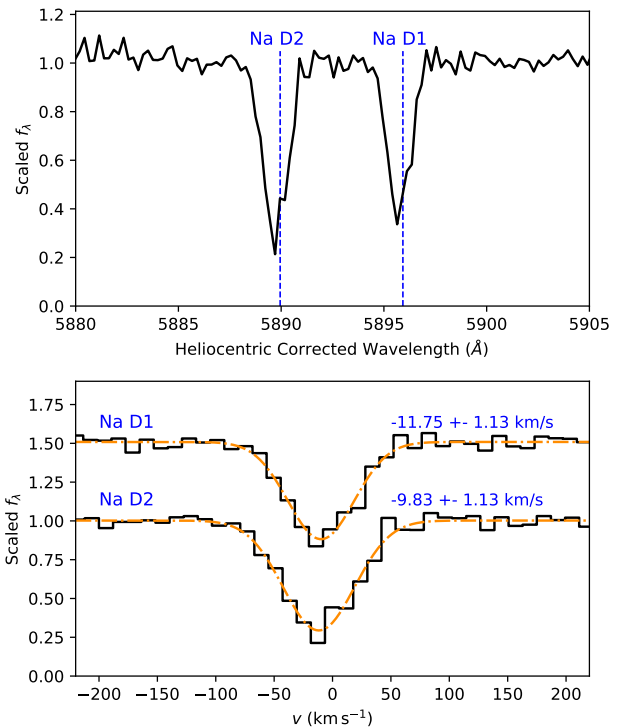


Figure 7. Zoom in on the Na I D lines of the ESI spectrum. *Upper:* Continuum normalized spectrum. *Lower:* Spectral lines in velocity space fitted with a Gaussian (dash-dotted lines).

In Section 4.1.2, we find that AT2019wey should have an extinction of $0.8 \lesssim E(B - V) \lesssim 1.2 \text{ mag}$. If this is from diffuse interstellar absorption, the distance of AT2019wey should be greater than 1 kpc using the map of SStructuring by Inversion the Local Interstel-

lar Medium (Stilism³; Capitanio et al. 2017), or greater than ~ 3 kpc using the 3D Dust Mapping constructed by Green et al. (2019)⁴. In addition, since AT2019wey is in the Galactic Anticenter direction (Table 1), the distance to AT2019wey is likely less than ~ 10 kpc.

We are able to put a lower limit to the distance of AT2019wey using the velocity of the Na I D doublets, given that the lines arise from interstellar absorption by a dust cloud along the line-of-sight to AT2019wey. The velocities of D1 and D2 lines are measured to be $-11.75 \pm 1.13 \text{ km s}^{-1}$ and $-9.83 \pm 1.13 \text{ km s}^{-1}$, respectively (see Figure 7). Assuming that the velocity of the dust cloud follows Galactic rotation, we have

$$V_{\text{obs,r}} = A d \sin(2l) \quad (5)$$

where $A = 15.3 \pm 0.4 \text{ km s}^{-1} \text{ kpc}^{-1}$ is the Oort A constant (Bovy 2017), $l = 151.16117^\circ$ (Table 1) is the Galactic longitude of AT2019wey, and d is distance to the dust cloud. Therefore, Eq. (5) gives $d = 0.83 \text{ kpc}$.

Taken together, we conclude that the distance of AT2019wey is between ~ 1 kpc to ~ 10 kpc. We note that if the object continues to remain sufficiently bright in the optical for an extended period of time, the next data release of the *Gaia* mission may help further constrain the distance.

4.2. NIR Spectroscopy

The NIR spectrum of AT2019wey is shown in Figure 8. Hydrogen emission lines of Pa γ , Pa β , and Br γ are clearly distinguished. We tentatively attribute the emission lines around 1083 nm to double-peaked He I. No absorption lines or molecular bands from the secondary star can be identified. With FWHM $\approx 200\text{--}300 \text{ km s}^{-1}$, the velocities of NIR emissions are much narrower than the H α emission, hinting at different formation locations in the accretion disk.

5. Radio Observations

5.1. Archival Limits

AT2019wey was not detected in any archival radio database. The NRAO VLA Sky Survey (NVSS, Condon et al. 1998) provides an upper limit of 2 mJy at 1.4 GHz in 1993–1996. The Karl G. Jansky Very Large Array Sky Survey (VLASS, Lacy et al. 2020) provides a $3\text{-}\sigma$ upper limit of 0.40 mJy at 2–4 GHz in Mar 2019.

5.2. Radio Observations

Table 9. Radio observations of AT2019wey.

Date	ν_0 (GHz)	f_ν (μJy)	α
2020-05-27	5.0	197 ± 20	0.51 ± 0.69
	6.0	220 ± 22	
	7.0	234 ± 23	
2020-08-02	2.5	218 ± 49	-0.82 ± 0.23
	3.5	205 ± 16	
	10.0	82 ± 11	
	11.5	1431 ± 13	
2020-08-14	1.5	1023 ± 75	0.23 ± 0.02
	2.5	998 ± 59	
	3.5	1077 ± 18	
	8.5	1420 ± 12	
	9.5	1399 ± 11	
	10.5	1447 ± 13	
2020-08-21	1.5	1676 ± 102	0.19 ± 0.01
	2.5	1767 ± 51	
	3.5	1923 ± 18	
	8.5	2340 ± 18	
	9.5	2393 ± 18	
	10.5	2376 ± 18	
2020-08-28	1.5	1846 ± 128	0.20 ± 0.01
	2.5	1891 ± 34	
	3.5	2048 ± 15	
	8.5	2529 ± 11	
	9.5	2542 ± 16	
	10.5	2536 ± 18	
2020-10-17	11.5	2511 ± 20	—
	6.7	1350 ± 220	

NOTE— ν_0 is central frequency. α is the spectral index defined as $f_\nu \propto \nu^\alpha$. The uncertainties are calculated using the 90% quantiles from the MCMC run.

We monitored AT2019wey in radio-band using the VLA (Perley et al. 2011). The observation was carried out under Director’s Discretionary Time (Program ID 20A-591, 20B-397; PI Y. Yao). AT2019wey was observed in S- and X-band on 2020 Aug 2, and in L-, S-, and X-band on Aug 14, Aug 21, and Aug 28. The data were calibrated using the standard VLA Pipeline. We present the flux density of our VLA detections in Table 9. Cao et al. (2020a) reported VLA C-band observations obtained on 2020 May 27. We fit a power-law function ($f_\nu \propto \nu^\alpha$) to the VLA data at each epoch using the Markov chain Monte Carlo (MCMC) approach with emcee (Foreman-Mackey et al. 2013). The fitting

³ <https://stilism.obspm.fr/>

⁴ <http://argonaut.skymaps.info/>

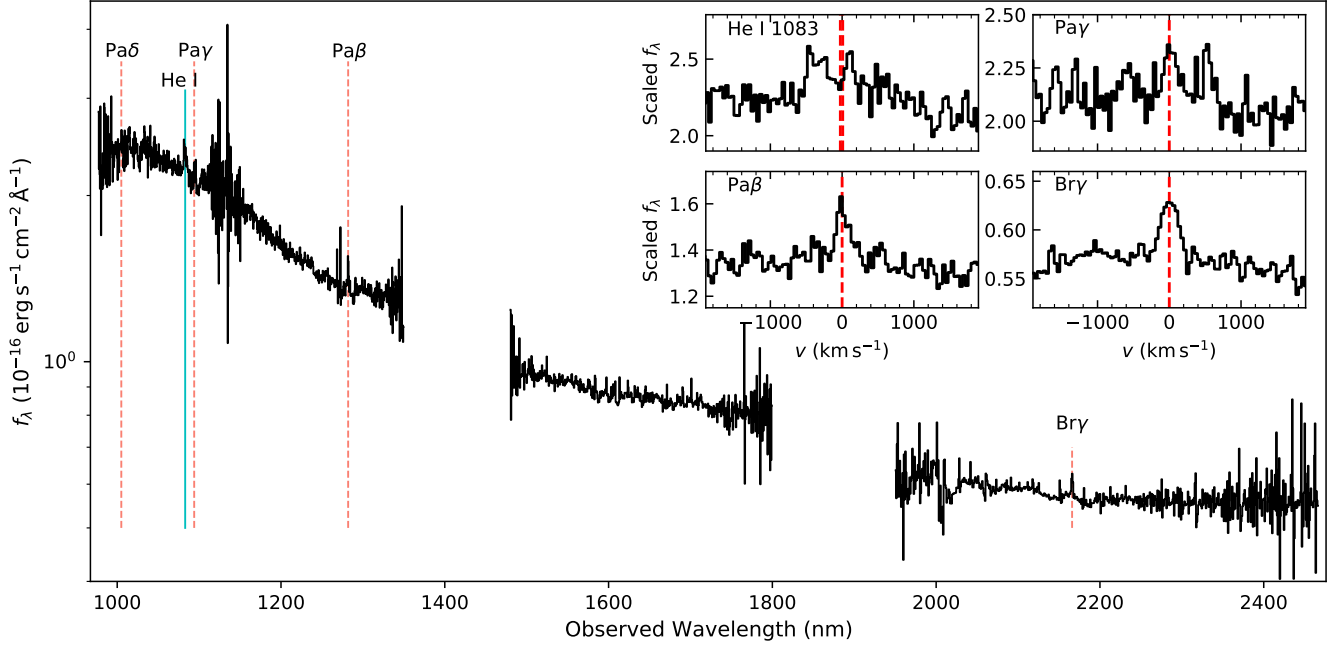


Figure 8. NIRES spectrum of AT2019wey. The insets show the zoom in on emission lines in velocity space.

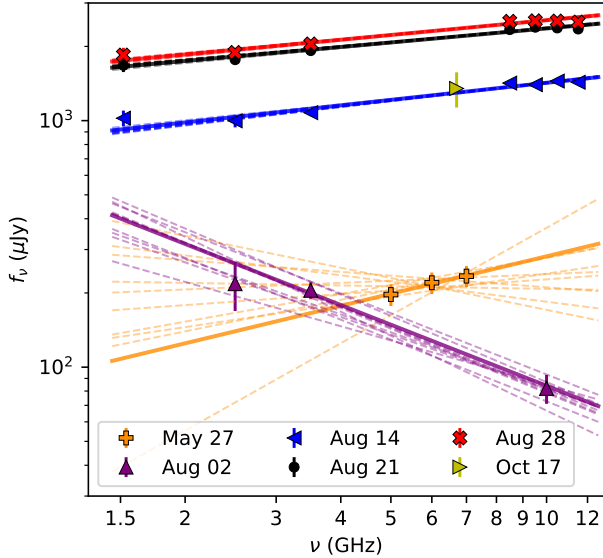


Figure 9. Radio observations of AT2019wey. The solid lines are model fits using estimated parameters. Ten random draws from the MCMC posterior are shown with dashed lines. Note that the random draws for the well constrained models (Aug 14, Aug 21, Aug 28) are so well aligned that they cannot be seen.

is shown in Figure 9, and the fitted spectral index α is shown in Table 9. Additionally, Cao et al. (2020b) reported 6.7 GHz observation taken with the European VLBI Network (EVN) obtained on 2020 Oct 17.

On May 27, Aug 14, 21, and 28, a flat or slightly inverted ($\alpha \approx 0-0.5$) radio spectrum was observed, which

can be explained by partially self-absorbed synchrotron emission from a conical, collimated jet (Blandford & Königl 1979; Kaiser 2006), as commonly detected in the LHS of X-ray binaries and quasar jet cores (Fender 2001). On Aug 2, however, a steep spectrum with $\alpha \sim -0.8$ was observed, which might arise from the optically thin synchrotron emission. The change of spectral index may indicate the existence of a multi-zone jet. Note that AT2019wey has transitioned to the HIM on Aug 28, indicating that there is no sign of jet suppression while the X-ray spectrum is softening.

6. Panchromatic Analysis

6.1. Radio-X-ray Correlation

To compare the radio and X-ray luminosities of AT2019wey with other X-ray binaries, we place AT2019wey on the L_{radio} versus L_{X} diagram in Figure 10. We have simultaneous radio and X-ray observations on Aug 14 (*NICER* OBSID = 3201710110), Aug 21 (OBSID = 3201710117), and Aug 28 (OBSID = 3201710124), shown in blue, black, and red, respectively. The Aug 2 radio observation has no simultaneous X-ray observation. Assuming that X-ray flux increased from Apr to Aug 9 (as indicated by the *MAXI* observations in Figure 11), we use the Aug 9 *NICER* observation (OBSID = 3201710105) to place an upper limit on its Aug 2 X-ray luminosity, and use the April *Swift* and *NuSTAR* observations to place a lower limit on its Aug 2 X-ray luminosity, as indicated by the dotted black lines. The radio 5 GHz luminosity is scaled as

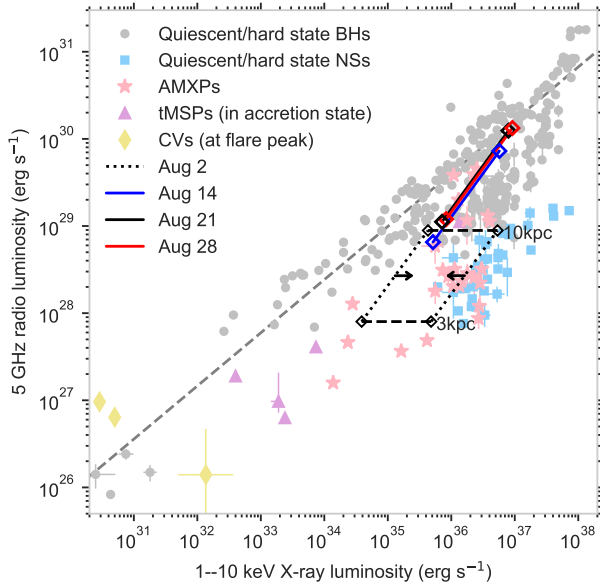


Figure 10. The radio versus X-ray correlation for the populations of X-ray sources. The dashed grey line shows the best-fit relation for BHs ($L_{\text{radio}} \propto L_X^{0.61}$, Gallo et al. 2006). We mark the positions of AT2019wey at four epochs for possible distances of 3–10 kpc.

suming a power-law spectrum (Figure 9 and Table 9). The X-ray 1–10 keV luminosity is derived from spectral fitting (see Paper I for details). Data from the literature on other BHs, NSs, accreting millisecond X-ray pulsars (AMXPs), transitional millisecond pulsars (tMSPs), and CVs are also indicated (Bahramian et al. 2018)⁵.

As shown in Figure 10, the radio and X-ray luminosities of AT2019wey are much brighter than that of CVs at flare peak. This indicates that AT2019wey is an X-ray binary system with a BH or NS accretor, consistent with its X-ray properties presented in Paper I.

6.2. Multi-wavelength Light Curve

6.2.1. Five Stages

The multi-wavelength light curve of AT2019wey is shown in the upper panel of Figure 11, which can be separated into five stages: (i) Before ~ 58814 MJD, the source was in quiescence, where the mass accretion rate was extremely low; (ii) From ~ 58814 MJD to ~ 58880 MJD, the optical light curve exhibited a fast-rise linear-decay outburst with peak flux of $f_{\nu,r} \sim 410 \mu\text{Jy}$, after which it settled onto $f_{\nu,r} \sim 315 \mu\text{Jy}$. Around the same time, the X-ray rose to ~ 1 mCrab, and no bright X-ray outburst righter than ~ 5 mCrab was ob-

served by *MAXI* and *Swift*/BAT (Paper I); (iii) From ~ 58880 MJD to ~ 59005 MJD, the optical and X-ray light curves stayed almost flat in the LHS; (iv) From ~ 59005 MJD to ~ 59080 MJD, AT2019wey exhibited a multi-wavelength brightening, and the X-ray remained in the LHS (Paper I); (v) From ~ 59075 MJD to the end of Oct 2020, optical stayed around $f_{\nu,r} \sim 400 \mu\text{Jy}$. Hard X-ray stays around ~ 25 mCrab, while soft X-ray went into a few bumps (Paper I). X-ray spectral-timing properties suggest that the source entered into the HIMS (Paper I).

6.2.2. UVOIR–X-ray Correlation

It is clearly manifested that during stage (iv), the X-ray and radio fluxes have increased by a factor of $\gtrsim 10$. However, the optical *r*-band and *g*-band fluxes increased only by factors of 1.3 and 1.4, respectively. Furthermore, the *U*-band ($\lambda_{\text{eff}} = 3475 \text{ \AA}$), *uvw1* ($\lambda_{\text{eff}} = 2614 \text{ \AA}$), *uvm2* ($\lambda_{\text{eff}} = 2255 \text{ \AA}$), and *uvw2* ($\lambda_{\text{eff}} = 2079 \text{ \AA}$) flux densities increased by factors of 2.2 ± 0.5 , 2.2 ± 0.6 , 2.0 ± 1.0 , and 3.7 ± 1.7 . Table 10 presents representative values of X-ray and optical luminosities at stage (iii) and stage (v). Following Russell et al. (2006), we approximate the optical luminosity by $L_{\text{opt}} \approx \nu f_{\nu}$. Parametrizing

$$L_{\text{opt}} = AL_X^{\beta}, \quad (6)$$

for AT2019wey, we find $\beta \sim 0.08$ in *r*-band, $\beta \sim 0.12$ in *g*-band, and $0.25 \lesssim \beta \lesssim 0.51$ in the UV band.

Global correlations between the optical and X-ray luminosities were previously found for LMXBs in the hard-state. Russell et al. (2006) derived $A = 10^{13.1 \pm 0.6}$, $\beta = 0.61 \pm 0.02$ for a sample of 15 BH LMXBs, and $A = 10^{10.8 \pm 1.4}$, $\beta = 0.63 \pm 0.04$ for a sample of 8 NS LMXBs. At $1 \lesssim D \lesssim 10$ kpc, the inferred luminosities of AT2019wey put it close to the hard-state BH LMXBs on the $L_{\text{opt}}-L_X$ diagram (Figure 12), while its optical luminosity is far above that expected for NS LMXBs. This suggests that the compact object in AT2019wey is probably a BH. Non-detection of pulsations in our extensive *NICER* monitoring (Paper I), as well as the hard X-ray spectrum obtained with the *Insight*/HXMT instrument (Tao et al. in prep) are in agreement with this inference.

6.2.3. Possible Mechanisms of the Optical Emission

The three dominating processes for the UV/optical emission of BH LMXBs in the LHS are thought to be: (1) Reprocessing of X-ray in the outer accretion disk; (2) Optically thick jet spectrum extended from the centimeter wavelength; (3) Intrinsic thermal emission from the viscously heated outer accretion disk. For X-ray reprocessing, the expected slope is $\beta \sim 0.5$ in the *V*-band (van

⁵ The data are downloaded from <https://github.com/bersavosh/XRB-LrLx-pub>

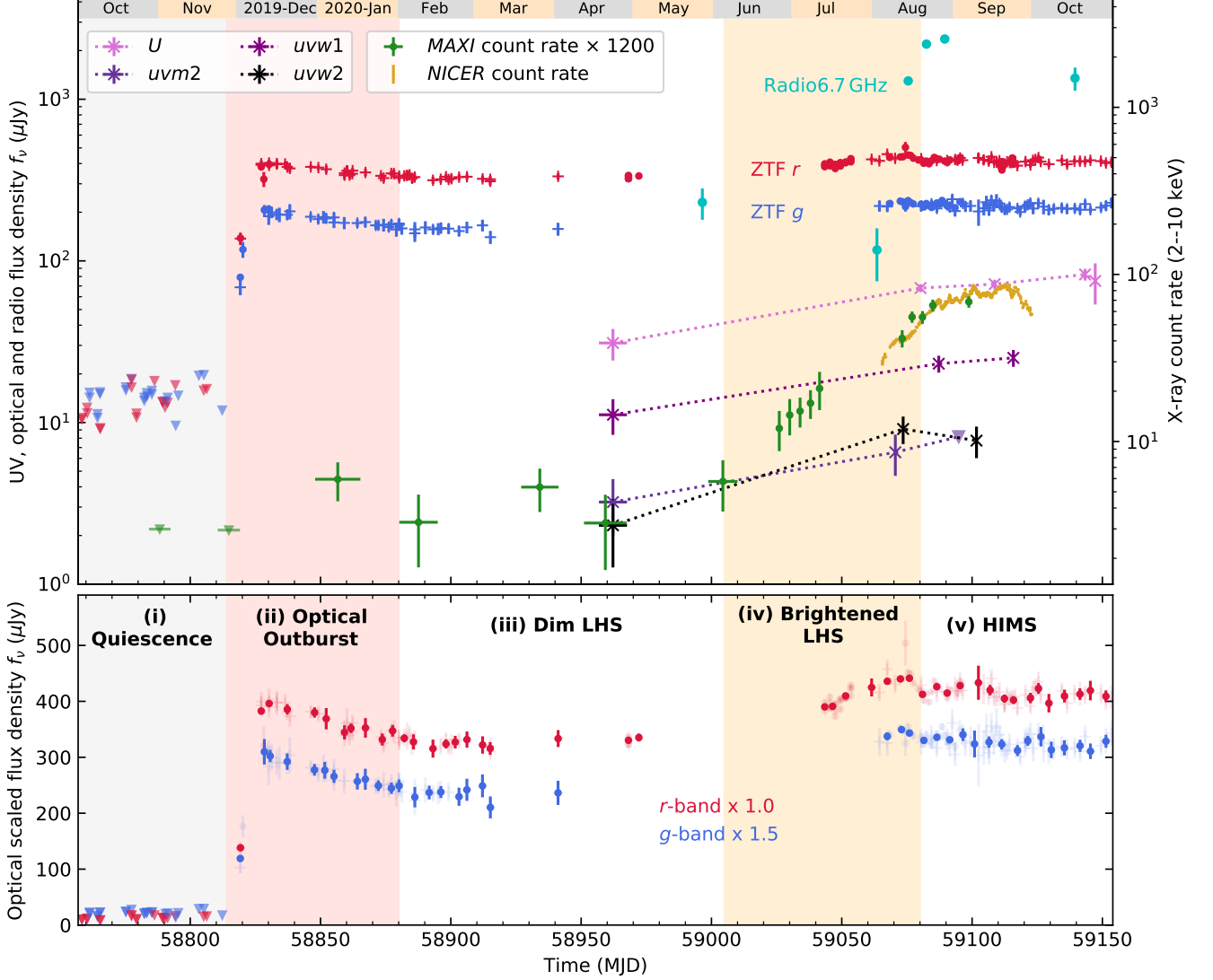


Figure 11. *Upper:* Observed multi-wavelength light curve of AT2019wey, including ZTF photometry and upper limits (Section 3.2.1 and Table 3), UV photometry and upper limits (Section 3.3 and Table 5), radio 6.7 GHz flux density interpolated from the radio spectra by the power-law fits (Section 5 and Table 9), and X-rays (Paper I). Radio, ZTF, and UV data are shown in units of flux density (left axis label), while X-ray data are shown in units of 2–10 keV count rate (the *MAXI* count rate has been scaled up to match the *NICER* count rate). The markers of ZTF data follow that shown in Figure 2. *Bottom:* The observed optical light curve of AT2019wey binned by 5 d is shown in linear scale with high-opacity colors, while the original data are shown in in semi-transparent. The *g*-band flux density has been multiplied by 1.5 for clarity.

Table 10. X-ray and optical luminosity of AT2019wey at different stages of the multi-wavelength evolution.

Stage	Band	Luminosity	Comments
(iii)	<i>r</i> & <i>g</i>	4.0×10^{34} & 6.1×10^{34}	Averaged between ~ 58880 MJD and ~ 59005 MJD
(iii)	X-ray	1.0×10^{35}	Averaged between ~ 58951 MJD and ~ 58967 MJD
(v)	<i>r</i> & <i>g</i>	4.9×10^{34} & 8.4×10^{34}	Averaged between ~ 59080 MJD and ~ 59153 MJD
(v)	X-ray	$(1.3\text{--}1.7) \times 10^{36}$	Range of values from minimum (~ 59082 MJD) to maximum (~ 59112 MJD)

NOTE—Luminosity is given in units of $(D/5 \text{ kpc})^2 \text{ erg s}^{-1}$. X-ray column density corrected luminosity is given in 2–10 keV, assuming $N_{\text{H}} = 5 \times 10^{21} \text{ cm}^{-2}$. Optical luminosity has been corrected for extinction, adopting $E(B - V) = 0.9$ mag

Paradijs & McClintock 1994), and increases (decreases) at shorter (longer) wavelength. For the optically thick

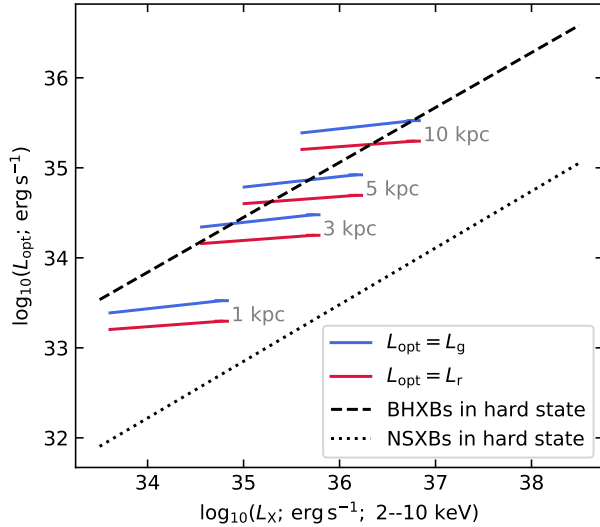


Figure 12. The solid lines demonstrate the correlation between optical (g - or r -band) and X-ray luminosities of AT2019wey from stage (iii) to stage (v), assuming distances at [1, 3, 5, 10] kpc. The dashed and dotted lines are best power-law fits to BH X-ray binaries (BHXBs) and NS X-ray binaries (NSXBs) in the hard state, respectively (Russell et al. 2006).

jet spectrum, $\beta \sim 0.7$ is expected (Corbel et al. 2003; Russell et al. 2006). For a viscously heated disk, the expected slope ranges from $\beta = 0.13$ (RJ tail) to $\beta = 0.33$ (between the RJ tail and the Wien cut-off) (Tetarenko et al. 2020). The correlation of $\beta \sim 0.6$ derived by Russell et al. (2006) suggest that irradiation and jet are the two processes contributing most to the optical emission of a large number of BH LMXBs. However, the observed $\beta \sim 0.1$ for AT2019wey suggests that intrinsic disk emission might play an important role here. We further investigate possible origins of the bright UV/optical emission in Section 6.3.

We note that small values of β have also been observed in a few other BH LMXBs in the LHS. For example, $\beta \sim 0.2$ is reported by Armas Padilla et al. (2013) during the outburst decay of Swift J1357.2–0933, a short-period system ($P_{\text{orb}} = 2.8$ h) with a $\sim 0.4 M_{\odot}$ companion star (Corral-Santana et al. 2013; Mata Sánchez et al. 2015); $\beta \sim 0.2$ was observed the outburst decay of Swift J1753.5–0127 (see Fig. 1 of Chiang et al. 2010), another short-period system ($P_{\text{orb}} \lesssim 3.244 \pm 0.001$ h) with a $\lesssim 0.3 M_{\odot}$ companion star (Zurita et al. 2008; Neustroev et al. 2014). Interestingly, the X-ray of both systems are only observed in the LHS or HIMS, without successful transitions to the high/soft state (HSS) (Armas Padilla et al. 2013; Shaw et al. 2016). These

similarities might be understood as characteristics for a sub-population of BH LMXBs (see Section 8).

6.3. Multi-wavelength SED

The spectral energy distribution (SED) of AT2019wey is shown in Figure 13.

6.3.1. The X-ray and Radio Spectrum

We perform X-ray spectral fitting using XSPEC version 12.11.0 (Arnaud 1996). See Paper I for details of X-ray observation and data reduction. Using the calibration of $N_{\text{H}} = 5.55 \times 10^{21} \times E(B-V)$ (Predehl & Schmitt 1995), the column density N_{H} is fixed at $5 \times 10^{21} \text{ cm}^{-2}$. We model the *Swift*/XRT data obtained in Apr 2020 with an absorbed PL (tbabs*powerlaw, in XSPEC, Wilms et al. 2000) with photon index $\Gamma \sim 1.8$. Paper I shows that a soft thermal component is observed after the X-ray brightening in stage (iv). Therefore, we fit the *NICER* data obtained on Aug 14, Aug 21, Aug 28, and Sep 20 with tbabs*simpl*diskbb. The dates are chosen to reflect representative X-ray spectra in stages (iv) and (v). Here diskbb is a multi-color accretion disk (Shakura & Sunyaev 1973; Mitsuda et al. 1984) and simpl is a Comptonization model that generates the PL component via Compton upscattering of seed photons from the accretion disk (Steiner et al. 2009). The column density corrected models are shown in Figure 13.

From Aug 14 to Aug 28, the fitted models generally exhibits PL photon index $\Gamma \sim 1.9$ and inner disk temperature $T_{\text{disk}} \sim 0.21 \text{ keV} \sim 2.4 \times 10^6 \text{ K}$. The inner disk radius can be obtained from the normalization term of the diskbb component

$$R_{\text{in}} \sim (360\text{--}470) \left(\frac{\cos i}{1} \right)^{-1/2} \left(\frac{D}{5 \text{ kpc}} \right) \text{ km}. \quad (7)$$

On Sep 20, the soft X-ray reaches a local maximum in the HIMS, where the PL has softened to $\Gamma = 2.3$ and the inner disk temperature has increased to $T_{\text{disk}} \sim 0.29 \text{ keV} \sim 3.4 \times 10^6 \text{ K}$, while the inner disk radius remains at $\sim 400 \text{ km}$. The fitted T_{disk} and R_{in} are typical for thermal emission of a truncated accretion disk observed in the LHS and HIMS of BH LMXBs (Done et al. 2007). Denoting the innermost stable circular orbit radius $R_{\text{ISCO}} = 6GM/c^2$ and the Schwarzschild radius $R_{\text{S}} = 2GM/c^2$, $R_{\text{in}} \sim 15R_{\text{S}} \sim 5R_{\text{ISCO}}$ of a $10 M_{\odot}$ non-spinning black hole.

The dash-dotted lines shown in Figure 13 are best-fits of the radio data (Table 9) extending to $3 \times 10^{12} \text{ Hz}$. If the spectrum remains optically thick all the way to the optical and near-infrared (OIR) wavelength, it will over-predict the observed OIR spectrum. Assuming a classical jet spectrum of a broken PL (Blandford & Königl

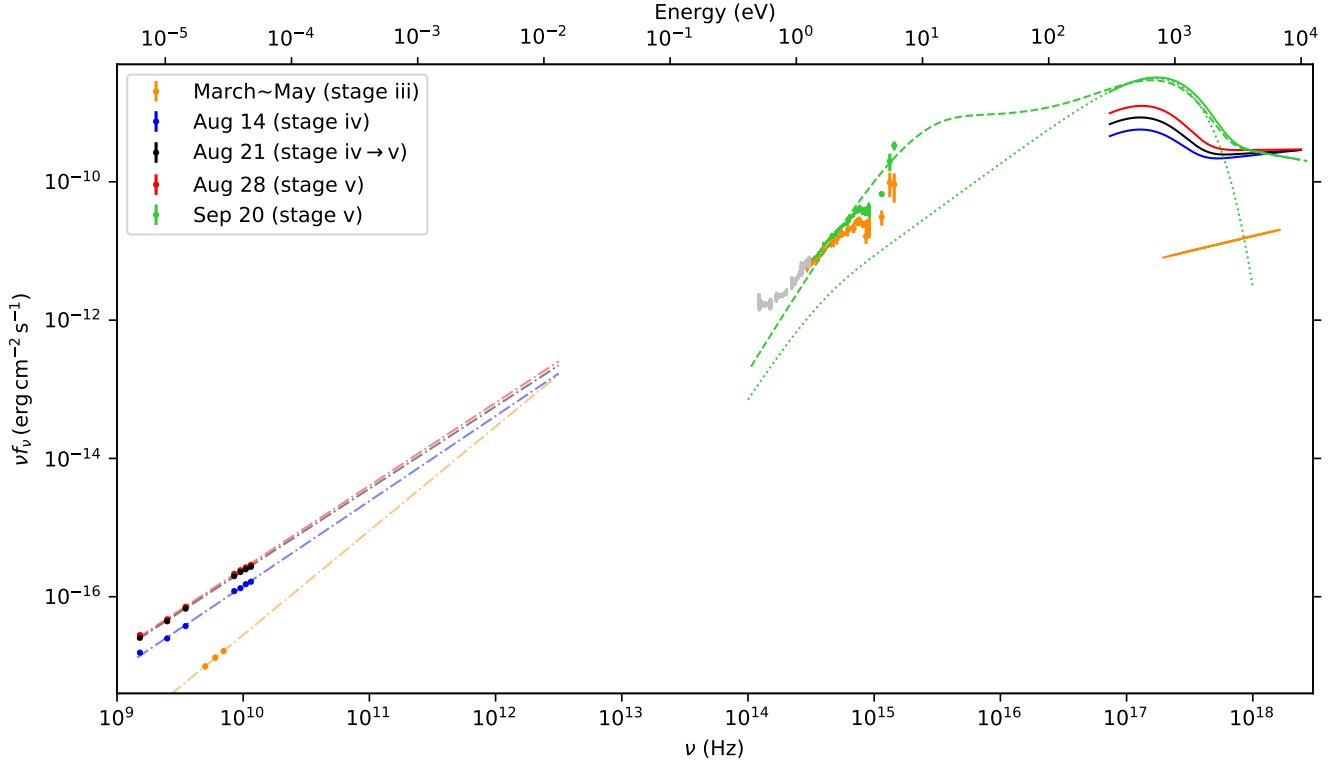


Figure 13. Multi-wavelength SED of AT2019wey. In radio, we show the observed data and power-law fits (Table 9). In UV/optical/NIR, we show the dereddened photometry and spectra assuming $E(B - V) = 0.9$ mag. Note that the silver NIR spectrum, the orange optical spectrum, and the green optical spectrum were obtained on Aug 13, March 20, and Sep 20, respectively (Table 6). In X-ray, we show the best-fits to X-ray data corrected for a fixed column density of $N_{\text{H}} = 5 \times 10^{21} \text{ cm}^{-2}$ (see Section 6.3.1 for details). See definition of different stages in the lower panel of Figure 11. The dashed and dotted green lines from optical to X-ray are illustrative models of irradiation and standard disk emission, respectively (see Section 6.3.3 for details).

1979), the break frequency must be $\ll 10^{14}$ Hz. The optically thin jet spectrum may contribute a fraction of NIR emission (grey data in Figure 13), but is unlikely to dominate in optical. This agrees with the inference presented in Section 6.2.3, that the $\beta \sim 0.1$ slope observed in AT2019wey is too small to be explained by jet emission. Therefore, in Section 6.3.2 and 6.3.3, only intrinsic emission of an accretion disk and X-ray reprocessing are considered as possible origins of the UV/optical emission.

6.3.2. UV/Optical Emission in the Dim LHS

In Figure 14, we show the UV/optical data and the best-fit X-ray model in the dim LHS (stage iii) in orange. The SED apparently come from two disjoint components. The X-ray is well-fitted by a PL with photon index $\Gamma \sim 1.8$, while the optical/UV continuum resembles the RJ tail of a blackbody. The detection of Balmer jump and broad Balmer absorption lines (Section 4.1) also implies that thermal emission contributed substantially to the optical band. The low level of X-ray

flux (compared to that in the UV/optical) suggests that there is not enough X-ray to illuminate the outer accretion disk. As a result, the UV/optical probably comes from the intrinsic thermal emission of an accretion disk.

To obtain a constraint of the outermost annulus of the accretion disk, we compute a set of simple blackbody models with T_{bb} fixed at 11000 K, 20000 K, and 25000 K (upper panel of Figure 14). All models are normalized to match the r -band photometry at 4.7×10^{14} Hz. The 11000 K model matches long-wavelength ($\lambda > 6000 \text{ \AA}$) data, but under-predict the near-UV (NUV) flux. The higher temperature models account for the NUV data well, but are generally below the observed SED at $\lambda > 6000 \text{ \AA}$. Next, we adopt the 11000 K blackbody as an approximation of the outer disk annulus, and compute a set of `diskbb` models to obtain a lower limit of the inner disk radius (and an upper limit of the inner disk temperature). The dotted line in the lower panel of Figure 14 suggests $T_{\text{in}} < 4.8 \times 10^5 \text{ K}$ and $R_{\text{in}} > 3.3 \times 10^3 \text{ km} \sim 38R_{\text{ISCO}} \sim 114R_{\text{S}}$. We note

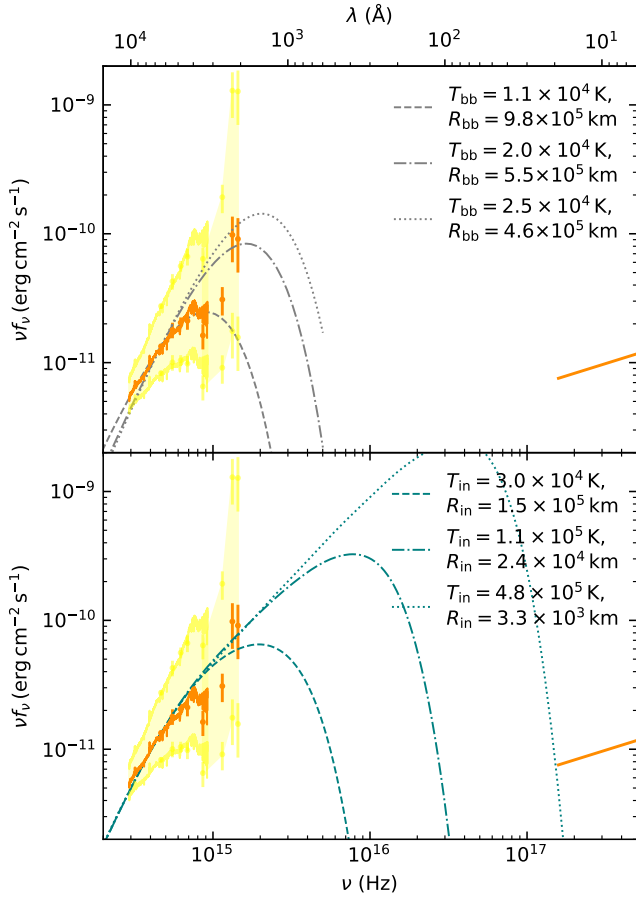


Figure 14. X-ray–UV–optical SED of AT2019wey in the dim LHS. The upper and lower bounds of the yellow region are obtained by dereddening the observed data using $E(B - V) = 1.2$ mag and 0.7 mag, respectively. Single-temperature blackbody models are shown in the upper panel, while disk-blackbody models are shown in the lower panel. All models are normalized to match the flux in r -band. $D = 5$ kpc and $\cos i = 1$ are assumed

that at $E(B - V) \sim 0.9$ mag, the transmission of the interstellar medium is very low in the UV ($< 1\%$ in $uvw2$, $uvm2$, and $uvw1$). Therefore, the extinction-corrected flux is highly susceptible to the uncertainty in $E(B - V)$ and the extinction law adopted here (Section 4.1.2), as demonstrated by the yellow region in Figure 14. Therefore, we do not perform detailed model fits, but emphasize that the UV/optical SED can be well explained by intrinsic thermal emission from a multi-color disk, where the inner disk radius is truncated far from the ISCO.

Similar SED shapes have been observed in the LHS of a few BH LMXBs, including XTE J1118+480 ($R_{\text{in}} = 300R_S$; Yuan et al. 2005) and Swift J1753.5–0127 ($R_{\text{in}} > 100R_S$; Froning et al. 2014). The observed SED of AT2019wey in the dim LHS fits into the picture of a hot accretion flow around a BH, which is predicted at

low-accretion rate (see reviews by Done et al. 2007; Yuan & Narayan 2014; Poutanen & Veledina 2014). The hot accretion flow is widely referred to as the advection-dominated accretion flow (ADAF; Narayan & Yi 1994, 1995). In such a scenario, the X-ray PL comes from a high-temperature flow in the central regions close to the BH, while the UV/optical thermal component comes from a geometrically thin, optically thick truncated accretion disk (Yuan & Narayan 2014).

6.3.3. UV/Optical Emission in the HIMS

The dotted green line in Figure 13 shows an extrapolation of the `diskbb` fit on *NICER* data for Sep 20. It clearly under-predicts the observed UV/optical spectrum, making X-ray reprocessing the most likely origin of the UV/optical emission in the HIMS. We therefore attempt to fit the green data by the irradiation model `diskir` (Gierliński et al. 2008, 2009).

We set the inner disk temperature of the unilluminated disk and the asymptotic power-law photon index the same as the best-fit Sep 20 model obtained in Section 6.3.1. The fraction of reprocessed luminosity in the Compton tail (f_{in}) is fixed at 0.1. The electron temperature is fixed at 1000 keV as there is no sign of a high-energy PL cutoff (see Paper I). The dashed green line in Figure 13 is a schematic fit with the following parameters: the ratio of luminosity in the Compton tail to that of the unilluminated disk $L_C/L_d = 0.22$, the radius of the Compton illuminated disk $R_{\text{irr}} = 1.2R_{\text{in}}$, the fraction of thermalized bolometric flux $f_{\text{out}} = 0.08$, $R_{\text{out}} = 10^{3.55}R_{\text{in}}$, and the normalization parameter of the unilluminated disk (Eq. 7) ≈ 370 km. We conclude that the UV/optical SED in the HIMS is consistent with being produced from X-ray irradiation.

6.3.4. Evolution of Optical Hydrogen Lines

In Section 6.3.3 and 6.3.2 we have shown that in the HIMS, the UV/optical emission comes from the reprocessing of inner disk and coronal emission. Irradiation of the outer disk may form a thin temperature-inversion layer on the disk surface (Tuchman et al. 1990). This naturally explains the enhanced Balmer emission lines observed during stage (iv) and stage (v) (Section 4.1.3).

7. Discussion

7.1. Constraint on Companion Stellar Mass

In Section 3.1, we present historical optical upper limits at the position of AT2019wey. The deep historical limits can provide constraints on the mass of the companion, assuming that the secondary is a hydrogen-burning main-sequence star. To this end, we convert the apparent limit magnitude in SDSS r' -band to absolute

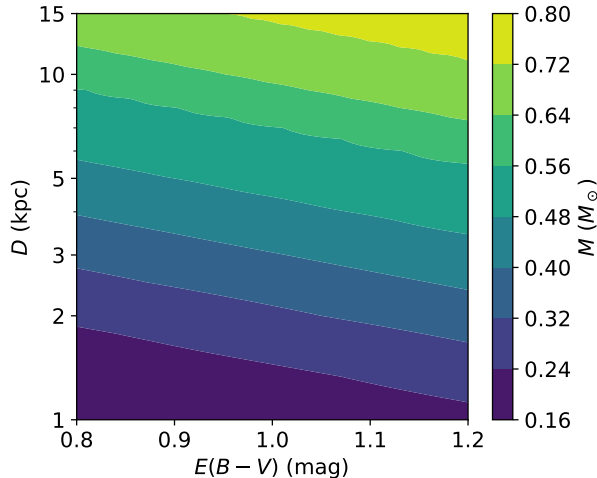


Figure 15. Upper limits of the companion mass assuming different values of $E(B - V)$ and distance (D).

limit magnitude with the following formula

$$\lim(M_{r'}) = \lim(m_{r'}) - A_{r'} - 10 - 5 \times \log_{10}(D_{\text{kpc}}) \quad (8)$$

where $\lim(m_{r'}) = 24.8$ mag (Table 2), D_{kpc} is the distance to AT2019wey in units of kpc, and $A_{r'} = 2.72 \times E(B - V)$ is the extinction in r' -band. We then convert $\lim(M_{r'})$ to an upper limit of the stellar mass of main-sequence dwarfs using the relation provided by Pecaut & Mamajek (2013, Table 5)⁶. Figure 15 shows the upper limits of the companion mass under ranges of possible extinction and distance. We conclude that the companion, should it be a main-sequence star, must be less heavy than $0.8 M_{\odot}$, and likely $< 0.5 M_{\odot}$. This firmly verifies that AT2019wey is a LMXB.

7.2. Constraint on Orbital Period

Shahbaz & Kuulkers (1998) presented an empirical relation between the optical outburst amplitude and P_{orb} for short-period LMXBs

$$\Delta V = 14.36 - 7.63 \log_{10} P_{\text{orb}}(\text{h}) \quad (9)$$

Assuming that $\Delta V(\lambda_{\text{eff}} = 551 \text{ nm}) \approx \Delta r(\lambda_{\text{eff}} = 642 \text{ nm})$, we have

$$\Delta V \approx \Delta r > (24.8 - 17.4) = 7.4 \text{ mag} \quad (10)$$

where 24.8 is the r' -band upper limit in quiescence (Table 2), and 17.4 mag is the r -band outburst magnitude

⁶ We downloaded an updated version of this table from http://www.pas.rochester.edu/~emamajek/EEM_dwarf_UBVIJHK_colors_Teff.txt.

(Figure 2). Plugging Eq. (10) into Eq. (9) implies $P_{\text{orb}} < 8.2$ h, providing an upper limit on the P_{orb} of AT2019wey. Below we search for periodicity in the optical data in Section 7.2.1, and discuss its validity and implication in Section 7.2.2.

7.2.1. Period Search

The ZTF Galactic deep drilling survey covered the field of AT2019wey on 2020-09-19 and 2020-09-23. On Sep 19 and Sep 23, we have 131 and 133 continuous exposures of over ~ 1.5 h, respectively (Figure 16). We search for periodicity on a frequency grid from 16 d^{-1} to 500 d^{-1} using the analysis of variance (AOV) method (Schwarzenberg-Czerny 1998)⁷. The solid black lines in Figure 17 show the periodograms for data taken on Sep 19, Sep 23, and both nights. To see how the observation cadence affect the periodogram, we utilize the `astropy` (Astropy Collaboration et al. 2013) implementation of the Lomb-Scargle algorithm (see a recent review by VanderPlas 2018) to compute the window function. In each panel of Figure 17, we show the window function with a dotted grey line, and mark the best period ($P = 1/\nu$) where the periodogram has the maximum value.

Similar to Burdge et al. (2020), we define “significance” as the maximum value in the periodogram divided by the standard deviation of values across the full periodogram. A period of $P = 1.27$ h at a significance of 9.1 was detected from the 2020-09-19 observation, while a period of 0.71 h at a low significance of 5.2 was identified using the 2020-09-23 observation. Using data from both nights, a period of 1.31 h can be detected with a significance of 9.7. For the identification of short-period binaries, Burdge et al. (2020) adopt significance > 8 as the threshold for eye-inspection (see their Appendix B). We therefore consider $P = 1.3$ h to be a good period candidate.

We also searched for periodicity in the CHIMERA data on a frequency grid from 1 d^{-1} to 100 d^{-1} , while no significant period can be identified. We note that AT2019wey exhibit intra-night variability of ~ 0.1 mag.

7.2.2. Discussion on the Periodicity

Ideally, for BH LMXBs, P_{orb} should be measured in quiescence when the secondary star dominates in optical, showing ellipsoidal modulation and/or radial velocity variation. Alternatively, for high-inclination systems in the outburst state, P_{orb} can also be constrained via spectroscopic analysis of the optical double-peaked emission line profile (Corral-Santana et al. 2013;

⁷ We utilize the `python` script provided by <https://users.camk.edu.pl/alex/#software>

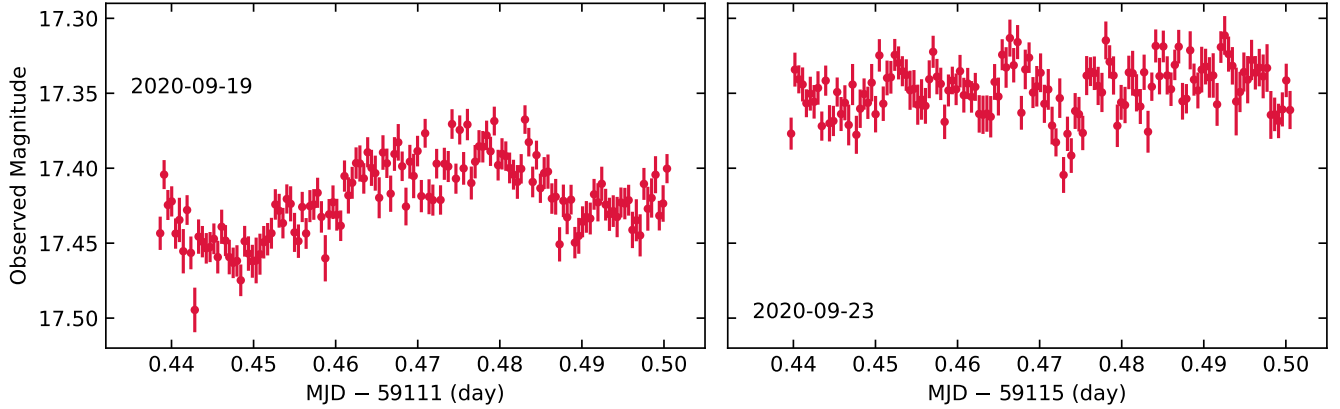


Figure 16. ZTF forced photometry light curve of AT2019wey on 2020-09-19 (left) and 2020-09-23 (right).

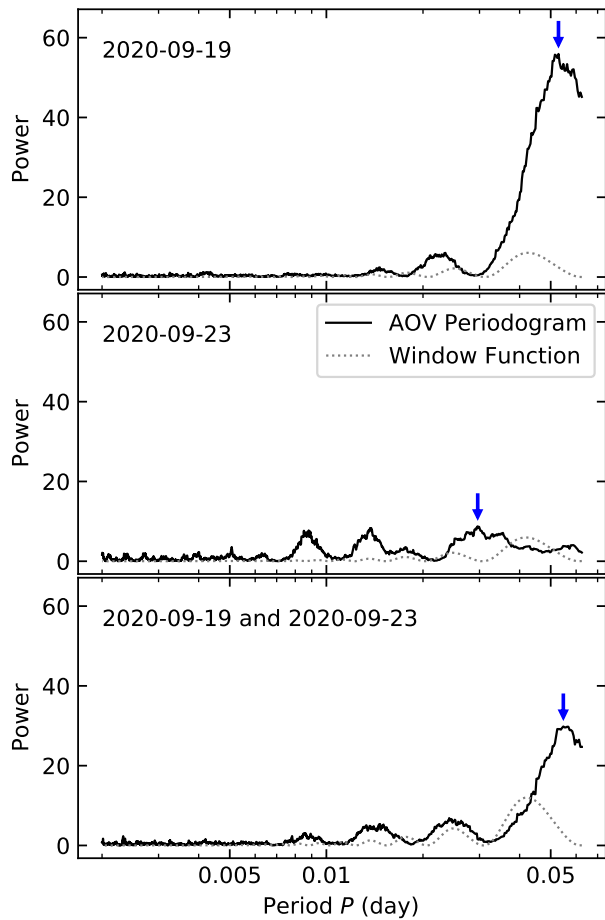


Figure 17. The AOV periodogram (solid black) and associated window function (dotted grey) for ZTF data on Sep 19 (upper), Sep 23 (middle), and both nights (bottom). In each panel, the best period is marked by the arrow.

Neustroev et al. 2014; Mata Sánchez et al. 2015) or orbital modulation in the optical/X-ray light curves (Kulkers et al. 2013; Corral-Santana et al. 2018). The above methodology is hard to apply in AT2019wey due to the faintness of the companion star and the low inclination of this system. However, we note that before $P_{\text{orb}} = 5.091850 \pm 0.000005$ h was dynamically established for the low-inclination BH LMXB GRO J0422+32 by Gelino & Harrison (2003), multiple studies reported the transient 5.1 h modulation in optical photometry (Chevalier & Ilovaisky 1992; Kato et al. 1993; Callanan et al. 1995), which was suggested to be related to the orbital period. Therefore, the ~ 1.3 h optical modulation could also be related to P_{orb} of AT2019wey, although more observations are needed for a conclusive measurement.

In the canonical theory of BH LMXB evolution, the binary system evolves to shorter period due to orbital angular momentum loss (Li 2015). In the population synthesis study for semidetached systems, Yungelson et al. (2006) predicted that systems with short period ($P_{\text{orb}} \leq 2$ h) and very low mass-ratio ($q = M_{\text{star}}/M_{\text{BH}} < 0.02$) might form the majority of the BH LMXB population. The authors suggest that these systems should be concentrated around a minimum P_{orb} at ~ 70 – 80 min. The existence of this sub-population of sources is not observed (Kneivt et al. 2014). A more reliable P_{orb} measurement for AT2019wey is needed to test the validity of the transient periodicity observed here, and to test formation theories of low-mass black hole binaries.

8. Conclusion

We have undertaken a detailed multi-wavelength follow-up of the X-ray transient AT2019wey. The observables suggest that AT2019wey is a new LMXB and a BH candidate, consistent with our analysis of the X-

ray observations (Paper I). The properties of this system are summarized below:

- (a) The extinction towards AT2019wey is constrained to be $0.8 \lesssim E(B-V) \lesssim 1.2$ mag, and the distance is constrained to be $1 \lesssim D \lesssim 10$ kpc.
- (b) We observe Balmer emission cores (FWHM $\lesssim 400 \text{ km s}^{-1}$) on top of broad (FWHM $\sim 2000\text{--}3000 \text{ km s}^{-1}$) absorption troughs, as well as Paschen and Brackett emission lines (FWHM $\sim 250 \text{ km s}^{-1}$).
- (c) The historical SDSS upper limit of $\text{lim}(r') = 24.8$ mag puts a constraint on the mass of the companion star of $M_{\text{star}} \lesssim 0.8 M_{\odot}$.
- (d) The r -band amplitude between quiescence and outburst is $\Delta r > 7.4$ mag, providing an upper limit on the orbital period $P_{\text{orb}} < 8.2$ h. A transient modulation at 1.3 h is observed, but awaits verification.
- (e) Multi-wavelength light curve of AT2019wey can be separated into five distinct stages, as illustrated in Figure 11. During stage (iv), the optical flux only increased by 1.3–1.4 despite the significant brightening in X-ray and radio by more than a factor of 10.
- (f) The SED evolution fits into the picture of a hot accretion flow consisting of an inner ADAF and a truncated disk, which is the widely-accepted model for short-period BH LMXBs in the hard state.
- (g) In the dim LHS, the UV/optical emission comes from intrinsic thermal emission of an accretion disk with $R_{\text{in}} > 100R_{\text{S}}$ and $T_{\text{in}} < 4.8 \times 10^5 \text{ K}$. In the HIMS, the truncation radius has moved inwards such that $R_{\text{in}} \sim 15R_{\text{S}}$ and $T_{\text{in}} \sim 0.3 \text{ keV}$. The dominate mechanism for the UV/optical emission is probably reprocessing of X-rays.

In recent years, more BH LMXBs with very short periods have been discovered. Among the 66 BH LMXBs presented in the updated BlackCAT⁸ catalog (Corral-Santana et al. 2016), five sources have carefully measured orbital periods less than 5 hours (MAXI 1659–152, Swift J1357.2–0933, Swift J1753.5–0127, XTE J1118+480, MAXI 1836–194). Except for MAXI 1659–152, the remaining four sources are all classified as “hard-only” outburst sources by

Tetarenko et al. (2016) — the X-ray light curve stays in the LHS for the entire outburst, or occasionally transitions to the HIMS, but never goes into the HSS. The “hard-only” outbursts are associated with lower mass accretion rates and lower peak X-ray luminosities (Wu et al. 2010; Tetarenko et al. 2016). These systems are relatively hard to identify with ASMs due to their faint X-ray flux. The *SRG* survey has the sensitivity to probe this sub-population in X-ray, and eROSITA’s small astrometry uncertainty ($\sim 5''$) makes it easy to search for counterparts at longer wavelength.

The optical outburst of AT2019wey is not accompanied by a bright X-ray nova outburst, which is a distinctive feature of AT2019wey. During the dim LHS lasting for ~ 0.5 yr, neither X-ray reprocessing nor synchrotron emission from jet outflow contributes significantly in optical. Instead, intrinsic thermal emission from a truncated accretion disk in the radiatively inefficient hot accretion flow makes the binary system appear as a bright transient in UV/optical. The discovery of AT2019wey showcase the possibility of hunting for similar systems in wide-field optical surveys. Perhaps the easiest approach to identify similar LMXBs is to look at optical light curves of *SRG* point sources in the Galactic plane.

Acknowledgments

We thank Jakob Nordin for a careful reading of this manuscript. YY is supported in part by the Heising-Simons Foundation. MMK acknowledges generous support from the David and Lucille Packard Foundation. ECB is supported in part by the NSF AAG grant 1812779 and grant #2018-0908 from the Heising-Simons Foundation.

This work is based on observations obtained with the Samuel Oschin Telescope 48 inch and the 60 inch Telescope at the Palomar Observatory as part of the Zwicky Transient Facility project. ZTF is supported by the National Science Foundation under grant No. AST-1440341 and a collaboration including Caltech, IPAC, the Weizmann Institute for Science, the Oskar Klein Center at Stockholm University, the University of Maryland, the University of Washington, Deutsches Elektronen-Synchrotron and Humboldt University, Los Alamos National Laboratories, the TANGO Consortium of Taiwan, the University of Wisconsin at Milwaukee, and Lawrence Berkeley National Laboratories. Operations are conducted by COO, IPAC, and UW.

SED Machine is based upon work supported by the National Science Foundation under Grant No. 1106171. This work was supported by the GROWTH project

⁸ See <http://www.astro.puc.cl/BlackCAT/index.php>.

funded by the National Science Foundation under Grant No 1545949.

References

- Alam, S., Albareti, F. D., Allende Prieto, C., et al. 2015, *ApJS*, 219, 12
- Armas Padilla, M., Degenaar, N., Russell, D. M., & Wijnand s, R. 2013, *MNRAS*, 428, 3083
- Arnaud, K. A. 1996, in *Astronomical Society of the Pacific Conference Series*, Vol. 101, *Astronomical Data Analysis Software and Systems V*, ed. G. H. Jacoby & J. Barnes, 17
- Astropy Collaboration, Robitaille, T. P., Tollerud, E. J., et al. 2013, *A&A*, 558, A33
- Bahramian, A., Miller-Jones, J., Strader, J., et al. 2018, *Radio/X-ray correlation database for X-ray binaries*, , , doi:10.5281/zenodo.1252036
- Bellm, E. C., & Sesar, B. 2016, *pyraf-dbsp: Reduction pipeline for the Palomar Double Beam Spectrograph*, , , ascl:1602.002
- Bellm, E. C., Kulkarni, S. R., Barlow, T., et al. 2019a, *PASP*, 131, 068003
- Bellm, E. C., Kulkarni, S. R., Graham, M. J., et al. 2019b, *PASP*, 131, 018002
- Belloni, T. M., Motta, S. E., & Muñoz-Darias, T. 2011, *Bulletin of the Astronomical Society of India*, 39, 409
- Blagorodnova, N., Neill, J. D., Walters, R., et al. 2018, *PASP*, 130, 035003
- Blandford, R. D., & Königl, A. 1979, *ApJ*, 232, 34
- Boller, T., Freyberg, M. J., Trümper, J., et al. 2016, *A&A*, 588, A103
- Bovy, J. 2017, *MNRAS*, 468, L63
- Burdge, K. B., Prince, T. A., Fuller, J., et al. 2020, *arXiv e-prints*, arXiv:2009.02567
- Callanan, P. J., Garcia, M. R., McClintock, J. E., et al. 1995, *ApJ*, 441, 786
- Cao, H., Frey, S., Gabanyi, K., et al. 2020a, *The Astronomer’s Telegram*, 13984, 1
- Cao, H., Giroletti, M., Migliori, G., & Frey, S. 2020b, *The Astronomer’s Telegram*, 14168, 1
- Capitanio, L., Lallement, R., Vergely, J. L., Elyajouri, M., & Monreal-Ibero, A. 2017, *A&A*, 606, A65
- Cardelli, J. A., Clayton, G. C., & Mathis, J. S. 1989, *ApJ*, 345, 245
- Cenko, S. B., Fox, D. B., Moon, D.-S., et al. 2006, *PASP*, 118, 1396
- Chevalier, C., & Ilovaisky, S. A. 1992, *IAUC*, 5644, 2
- Chiang, C. Y., Done, C., Still, M., & Godet, O. 2010, *MNRAS*, 403, 1102
- Condon, J. J., Cotton, W. D., Greisen, E. W., et al. 1998, *AJ*, 115, 1693
- Corbel, S., Nowak, M. A., Fender, R. P., Tzioumis, A. K., & Markoff, S. 2003, *A&A*, 400, 1007
- Corral-Santana, J. M., Casares, J., Muñoz-Darias, T., et al. 2016, *A&A*, 587, A61
- . 2013, *Science*, 339, 1048
- Corral-Santana, J. M., Torres, M. A. P., Shahbaz, T., et al. 2018, *MNRAS*, 475, 1036
- Cushing, M. C., Vacca, W. D., & Rayner, J. T. 2004, *PASP*, 116, 362
- Dekany, R., Smith, R. M., Riddle, R., et al. 2020, *Publications of the Astronomical Society of the Pacific*, 132, 038001
- Done, C., Gierliński, M., & Kubota, A. 2007, *A&A Rv*, 15, 1
- Dubus, G., Kim, R. S. J., Menou, K., Szkody, P., & Bowen, D. V. 2001, *ApJ*, 553, 307
- Fender, R. P. 2001, *MNRAS*, 322, 31
- Flewelling, H. A., Magnier, E. A., Chambers, K. C., et al. 2016, *arXiv e-prints*, arXiv:1612.05243
- Foreman-Mackey, D., Hogg, D. W., Lang, D., & Goodman, J. 2013, *Publications of the Astronomical Society of the Pacific*, 125, 306
- Fremling, C., Sollerman, J., Taddia, F., et al. 2016, *A&A*, 593, A68
- Froning, C. S., Maccarone, T. J., France, K., et al. 2014, *ApJ*, 780, 48
- Gallo, E., Fender, R. P., Miller-Jones, J. C. A., et al. 2006, *MNRAS*, 370, 1351
- Gehrels, N., Chincarini, G., Giommi, P., et al. 2004, *ApJ*, 611, 1005
- Gelino, D. M., & Harrison, T. E. 2003, *ApJ*, 599, 1254
- Gendreau, K. C., Arzoumanian, Z., Adkins, P. W., et al. 2016, in *Society of Photo-Optical Instrumentation Engineers (SPIE) Conference Series*, Vol. 9905, *Space Telescopes and Instrumentation 2016: Ultraviolet to Gamma Ray*, 99051H
- Gierliński, M., Done, C., & Page, K. 2008, *MNRAS*, 388, 753
- . 2009, *MNRAS*, 392, 1106
- Graham, M. J., Kulkarni, S. R., Bellm, E. C., et al. 2019, *arXiv e-prints*, arXiv:1902.01945
- Green, G. M., Schlafly, E., Zucker, C., Speagle, J. S., & Finkbeiner, D. 2019, *ApJ*, 887, 93
- Harding, L. K., Hallinan, G., Milburn, J., et al. 2016, *MNRAS*, 457, 3036
- Hobbs, L. M., York, D. G., Snow, T. P., et al. 2008, *ApJ*, 680, 1256
- Horne, K., & Marsh, T. R. 1986, *MNRAS*, 218, 761
- Jenniskens, P., & Desert, F. X. 1994, *A&AS*, 106, 39
- Kaiser, C. R. 2006, *MNRAS*, 367, 1083
- Kasliwal, M. M., Cannella, C., Bagdasaryan, A., et al. 2019, *PASP*, 131, 038003

- Kato, T., Mineshige, S., & Hirata, R. 1993, *IAUC*, 5704, 1
 Kneivitt, G., Wynn, G. A., Vaughan, S., & Watson, M. G. 2014, *MNRAS*, 437, 3087
- Kuulkers, E., Kouveliotou, C., Belloni, T., et al. 2013, *A&A*, 552, A32
- La Dous, C. 1989, *A&A*, 211, 131
- Lacy, M., Baum, S. A., Chandler, C. J., et al. 2020, *PASP*, 132, 035001
- Law, N. M., Kulkarni, S. R., Dekany, R. G., et al. 2009, *PASP*, 121, 1395
- Li, X.-D. 2015, *NewAR*, 64, 1
- Lupton, R., Blanton, M. R., Fekete, G., et al. 2004, *PASP*, 116, 133
- Masci, F. J., Laher, R. R., Rusholme, B., et al. 2019, *PASP*, 131, 018003
- Mata Sánchez, D., Muñoz-Darias, T., Casares, J., Corral-Santana, J. M., & Shahbaz, T. 2015, *MNRAS*, 454, 2199
- Matsuoka, M., Kawasaki, K., Ueno, S., et al. 2009, *PASJ*, 61, 999
- McClintock, J. E., & Remillard, R. A. 2006, *Black hole binaries*, Vol. 39, 157–213
- Mereminskiy, I., Medvedev, P., Semena, A., et al. 2020, *The Astronomer’s Telegram*, 13571, 1
- Merloni, A., Predehl, P., Becker, W., et al. 2012, arXiv e-prints, arXiv:1209.3114
- Minkowski, R. L., & Abell, G. O. 1963, *The National Geographic Society-Palomar Observatory Sky Survey*, ed. K. A. Strand, 481
- Mitsuda, K., Inoue, H., Koyama, K., et al. 1984, *PASJ*, 36, 741
- Narayan, R., & Yi, I. 1994, *ApJL*, 428, L13
 —. 1995, *ApJ*, 452, 710
- Negoro, H., Kohama, M., Serino, M., et al. 2016, *PASJ*, 68, S1
- Neustroev, V. V., Veledina, A., Poutanen, J., et al. 2014, *MNRAS*, 445, 2424
- Oke, J. B., & Gunn, J. E. 1982, *PASP*, 94, 586
- Oke, J. B., Cohen, J. G., Carr, M., et al. 1995, *PASP*, 107, 375
- Patterson, M. T., Bellm, E. C., Rusholme, B., et al. 2019, *PASP*, 131, 018001
- Pavlinksky, M., Levin, V., Akimov, V., et al. 2018, in *Society of Photo-Optical Instrumentation Engineers (SPIE) Conference Series*, Vol. 10699, Proc. SPIE, 106991Y
- Pecaut, M. J., & Mamajek, E. E. 2013, *ApJS*, 208, 9
- Perley, D. A. 2019, *PASP*, 131, 084503
- Perley, R. A., Chandler, C. J., Butler, B. J., & Wrobel, J. M. 2011, *ApJL*, 739, L1
- Poutanen, J., & Veledina, A. 2014, *SSRv*, 183, 61
- Poznanski, D., Prochaska, J. X., & Bloom, J. S. 2012, *MNRAS*, 426, 1465
- Predehl, P., & Schmitt, J. H. M. M. 1995, *A&A*, 500, 459
- Predehl, P., Andritschke, R., Arefiev, V., et al. 2020, arXiv e-prints, arXiv:2010.03477
- Rahoui, F., Tomsick, J. A., Coriat, M., et al. 2015, *ApJ*, 810, 161
- Rau, A., Kulkarni, S. R., Law, N. M., et al. 2009, *PASP*, 121, 1334
- Reid, I. N., Brewer, C., Brucato, R. J., et al. 1991, *PASP*, 103, 661
- Remillard, R. A., & McClintock, J. E. 2006, *ARA&A*, 44, 49
- Rigault, M., Neill, J. D., Blagorodnova, N., et al. 2019, arXiv e-prints, arXiv:1902.08526
- Roming, P. W. A., Kennedy, T. E., Mason, K. O., et al. 2005, *SSRv*, 120, 95
- Russell, D. M., Fender, R. P., Hynes, R. I., et al. 2006, *MNRAS*, 371, 1334
- Russell, T. D., Soria, R., Motch, C., et al. 2014, *MNRAS*, 439, 1381
- Schlaflly, E. F., & Finkbeiner, D. P. 2011, *ApJ*, 737, 103
- Schwarzenberg-Czerny, A. 1998, *Baltic Astronomy*, 7, 43
- Shahbaz, T., & Kuulkers, E. 1998, *MNRAS*, 295, L1
- Shakura, N. I., & Sunyaev, R. A. 1973, *A&A*, 500, 33
- Shaw, A. W., Gandhi, P., Altamirano, D., et al. 2016, *MNRAS*, 458, 1636
- Soria, R., Wu, K., & Hunstead, R. W. 2000, *ApJ*, 539, 445
- Steiner, J. F., Narayan, R., McClintock, J. E., & Ebisawa, K. 2009, *PASP*, 121, 1279
- Tetarenko, B. E., Dubus, G., Marcel, G., Done, C., & Clavel, M. 2020, *MNRAS*, 495, 3666
- Tetarenko, B. E., Sivakoff, G. R., Heinke, C. O., & Gladstone, J. C. 2016, *ApJS*, 222, 15
- Tonry, J., Denneau, L., Heinze, A., et al. 2019, *Transient Name Server Discovery Report*, 2019-2553, 1
- Tonry, J. L., Denneau, L., Heinze, A. N., et al. 2018, *PASP*, 130, 064505
- Torres, M. A. P., Callanan, P. J., Garcia, M. R., et al. 2002, *ApJ*, 569, 423
- Truemper, J. 1982, *Advances in Space Research*, 2, 241
- Tuchman, Y., Mineshige, S., & Wheeler, J. C. 1990, *ApJ*, 359, 164
- Vacca, W. D., Cushing, M. C., & Rayner, J. T. 2003, *PASP*, 115, 389
- van Paradijs, J., & McClintock, J. E. 1994, *A&A*, 290, 133
- VanderPlas, J. T. 2018, *ApJS*, 236, 16
- Voges, W., Aschenbach, B., Boller, T., et al. 1999, *A&A*, 349, 389
- Warner, B. 1995, *Cataclysmic Variable Stars*, Cambridge Astrophysics (Cambridge University Press), doi:10.1017/CBO9780511586491
- Waters, C. Z., Magnier, E. A., Price, P. A., et al. 2016, arXiv e-prints, arXiv:1612.05245
- Wilms, J., Allen, A., & McCray, R. 2000, *ApJ*, 542, 914
- Wu, Y. X., Yu, W., Li, T. P., Maccarone, T. J., & Li, X. D. 2010, *ApJ*, 718, 620
- Yao, Y., Miller, A. A., Kulkarni, S. R., et al. 2019, *ApJ*, 886, 152
- Yuan, F., Cui, W., & Narayan, R. 2005, *ApJ*, 620, 905
- Yuan, F., & Narayan, R. 2014, *ARA&A*, 52, 529
- Yuan, H. B., & Liu, X. W. 2012, *MNRAS*, 425, 1763
- Yungelson, L. R., Lasota, J. P., Nelemans, G., et al. 2006, *A&A*, 454, 559

Zhang, S.-N. 2013, *Frontiers of Physics*, 8, 630

Zurita, C., Durant, M., Torres, M. A. P., et al. 2008, *ApJ*,
681, 1458